Injectable Polymer for *in vivo* Oxygen Sensing

by

Syed M. Imaad

B.S., Electrical Engineering
University of Illinois at Urbana-Champaign, 2010

Submitted to the Department of Electrical Engineering and Computer Science in Partial Fulfillment of the Requirements for the Degree of

Masters of Science in Electrical Engineering and Computer Science

at the

MASSACHUSETTS INSTITUTE OF TECHNOLOGY

February 2013

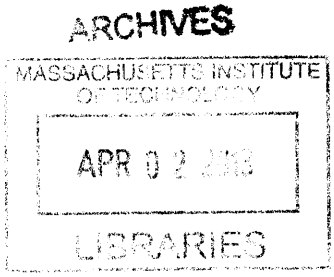

Signature of Author .....
Department of Electrical Engineering and Computer Science
December 28, 2012

Certified by .....
Michael J. Cima
David H. Koch Professor of Engineering
Thesis Supervisor

Accepted by .....
Leslie A. Kolodziejski
Professor of Electrical Engineering and Computer Science
Chair, EECS Committee on Graduate Students

Injectable Polymer for *in vivo* Oxygen Sensing

by

Syed M. Imaad

Submitted to the Department of Electrical Engineering and Computer Science on
December 28, 2012 in Partial Fulfillment of the
Requirements for the Degree of Masters of Science in
Electrical Engineering and Computer Science

ABSTRACT

This thesis documents the synthesis and characterization of an elastomeric polymer that is oxygen sensitive and can be interrogated using Magnetic Resonance Imaging (MRI) or Magnetic Resonance (MR) technology to report the oxygen tension *in vivo* at the site of implant. The polymer was tested for its sensitivity in response to oxygen, and the specificity of response to oxygen was verified. Oxygen diffusivity for this class of polymers was measured and correlated with the response sensitivity to oxygen to provide a possible explanation for the difference in response sensitivities within this class of polymers. Animal experiments were carried out in rats to test the performance of these sensors *in vivo* where device response to varying levels of inspired oxygen was monitored.

Thesis Supervisor: Michael J. Cima
Title: David H. Koch Professor of Engineering

Acknowledgments

I would like to thank my advisor, Professor Michael J. Cima, for providing me with the opportunity to work on a project that could have immense impact on clinical practice and in improving human life in the years to come. His guidance and valuable input over the course of my research has made it a worthwhile experience.

I would also like to thank the entire Cima Lab for being eagerly helpful and creating a great work environment. Special thanks to Vincent Liu and Christophorous Vassiliou for their help in research.

In the end I would like to thank my family, especially my parents Ambreen & Syed Tariq, for being a constant source of support and always providing me with the freedom to pursue my interests. They have had a large and perhaps most important role in the development of the individual I am today.

The work presented herein was made possible due to funding support of the National Cancer Institute's Center of Cancer Nanotechnology Excellence (5 U54 CA151884-03).

Table of Contents

Chapter 1: Introduction

1.1 Importance of *in vivo* oxygen measurements

Oxygen is an important molecule for a number of pathological and therapeutic processes. The delivery of oxygen to tissues is important in maintaining tissue function and survival [1]. The restriction in blood supply (hence oxygen) to tissue, more commonly known as ischemia, is known to be an underlying factor in pathologic conditions like cardiac dysfunction and wound healing [2].

Compartment Syndrome is yet another serious condition which can occur after ischemia followed by reperfusion in, for example, the limb. Compartment Syndrome is defined as a condition in which high pressure within a space reduces perfusion and tissue viability [3]. The anterior and deep posterior compartments of the leg are those most commonly affected [4]. Figure 1.1 shows a diagram of the four compartments of the leg and their positions, including the anterior and deep posterior compartments. Common causes of compartment syndrome include fractures, crush injuries and gunshot wounds [5]. Acute compartment syndrome can lead to amputation or even death if not treated early [6]. This is why it is of utmost importance to detect compartment syndrome at an early stage so it can be treated immediately, avoiding amputation or fatality. Compartment syndrome can be evaluated by measuring the intramuscular oxygen tension since compartment syndrome results in a decrease in microcirculation in the muscle tissue [7]. Measuring the oxygen tension becomes an attractive option for the early diagnosis of compartment syndrome where there is ischemic risk despite normal compartment pressures.

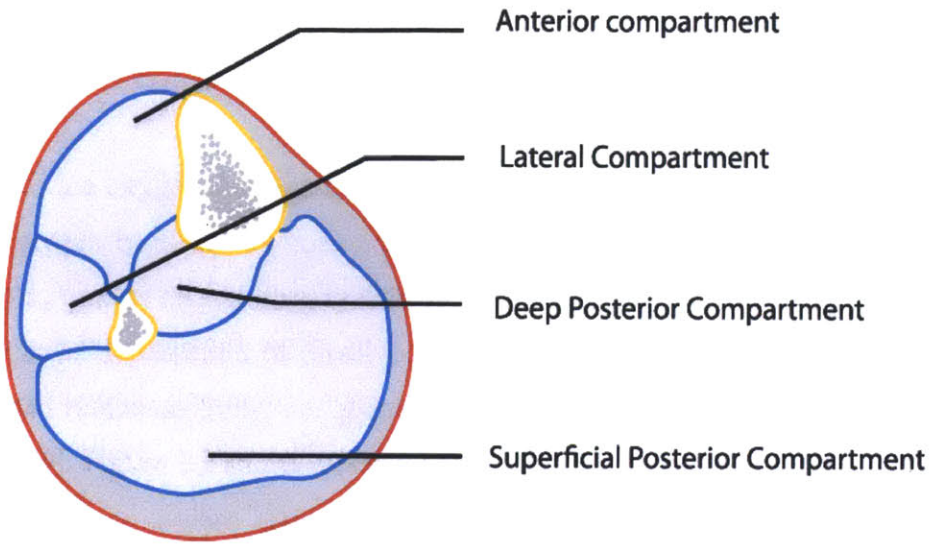

Figure 1.1 The four compartments of the leg (obtained from www.docpods.com/posterior-compartment-syndrome).

Measurement of the oxygen concentration is also significant in cancer therapy where the amount of dissolved oxygen in tumor microenvironments directly affects radiation treatment outcome. Hypoxia in solid tumors results from an imbalance between oxygen supply and consumption [8]. Tumor hypoxia, or depravation of dissolved oxygen in the vicinity of the tumor, is associated with a decreased radiosensitivity, i.e., greater radiation dose is required to treat hypoxic tumors and vice versa [9]. Figure 1.2 shows this correlation in a plot of biochemical non-evidence (or no evidence), or bNED, of disease against the prescription dose of ^{125}I brachytherapy as reported by Wang et al [10]. The monitoring of dissolved oxygen can therefore help clinicians in determining the appropriate radiation dosage that should be administered to a tumor patient. Vaupel et al. have demonstrated that measurements of oxygen tension using Clark microelectrodes help in determining the response of tumors to radiation therapy [11].

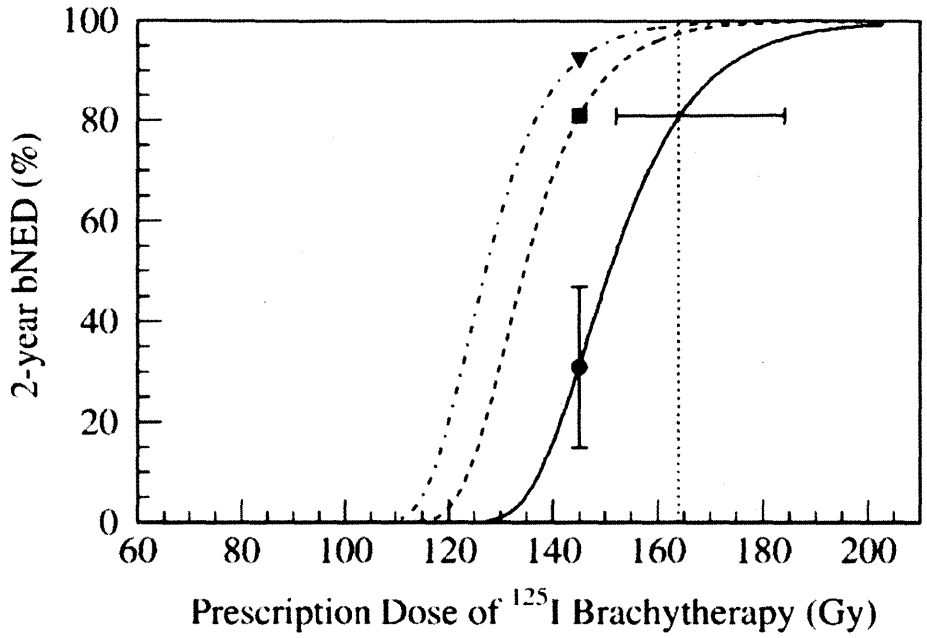

Figure 1.2 The 2-year bNED versus prescription dose of ^{125}I brachytherapy. Each line represents a different type of tumor: solid is hypoxic, dashed is non-hypoxic and dotted is aerated.

Some of the existing methods for determining oxygen concentration in tissues (explored in detail in Chapter 2) have their own limitations with respect to the inability of repeated measurements, the invasiveness of the procedure, and/or the inability to leverage existing standard clinical instrumentation and protocols. This thesis presents the development of a polymer material that can be formulated into an injectable device for oxygen sensing and overcomes the aforementioned limitations. The oxygen sensors that have been developed are biocompatible and synthesized using a similar class of materials used in breast implants. After the initial implant using a standard biopsy or injection needle, repeated and localized measurements can be made in a non-invasive manner. Such measurements are made possible by leveraging Magnetic Resonance Imaging (MRI) using standard pulse sequences. The fact that sensor readout is performed using a standard clinical imaging modality and protocol should reduce, if not eliminate, barriers to clinical translation of this diagnostic technology.

1.2 Thesis outline

Chapter 1 briefly described the importance of *in vivo* oxygen measurements, providing a precursor to Chapter 2 that presents a detailed review of existing technologies for such measurements. This review includes the existing clinical gold standards for *in vivo* oxygen sensing for conditions like compartment syndrome and tumor radiotherapy as well as technologies developed and reported in literature by other research groups. Chapter 3 explains some pertinent theoretical concepts related to Magnetic Resonance (MR) and how they apply to the measurement of oxygen concentration in conjunction with our implanted oxygen sensors. It presents important pulse sequences like Inversion Recovery (IR) and Saturation Recovery (SR) that have been used in the experiments performed, and includes pulse diagrams, relevant equations and essential parameters that are used in quantifying oxygen concentration. Chapter 4 describes the synthesis and response characteristics of the oxygen sensitive material, followed by Chapter 5 which presents oxygen diffusivity measurements and their correlation to the response sensitivity of the material to oxygen. Chapter 6 includes results of *in vivo* experiments obtained from pilot inspired gas animal studies. The thesis concludes with Chapter 7 by summarizing the reported work and a recommendation for future studies.

Chapter 2: Literature Review

Many different approaches for quantifying *in vivo* oxygen tension have been reported in literature. These various methods differ based on their invasiveness, repeatability, localization of measurement, and the principle of detection. This chapter reviews these approaches and is divided into two sections. Section 2.1 provides an overview of the existing clinical gold standards for (i) *in vivo* oxygen tension measurements in radiotherapy dose administration for tumor hypoxia; and (ii) compartment syndrome diagnosis. Section 2.2 discusses the development of *in vivo* oxygen sensors developed by other research groups based on principles such as fluorescence quenching, phosphorescence quenching, Electron Paramagnetic Resonance (EPR), contrast-enhanced Magnetic Resonance Imaging (MRI), Near-Infrared (NIR) spectrometry, and biopsy based methods. Advantages and potential limitations of these various approaches will be highlighted in order to better understand the need and importance of the work presented in this thesis.

2.1 Clinical gold standards

(i) Tumor Hypoxia

The optimal dosage required for radiotherapy depends on the extent of tumor oxygenation, as discussed in Chapter 1 earlier. The Eppendorf polarographic oxygen electrode based on the Clark electrode is the clinical gold standard for measuring tumor oxygenation [12]. It is essentially a needle electrode which comprises of a gold cathode (approximately 12 μm in diameter) that is insulated using a layer of glass and a silver-silver chloride anode that is attached to the surface of the skin. The tip of the gold cathode is covered by a Teflon membrane which is oxygen permeable and prevents biofouling. The oxygen tension is proportional to the concentration of oxygen which can be measured based on the oxidation-reduction reactions taking place at the two electrodes. Figure 2.1 shows an Eppendorf polarographic electrode as used for determining the tumor oxygenation in the neck of a patient with hypopharyngeal cancer [13].

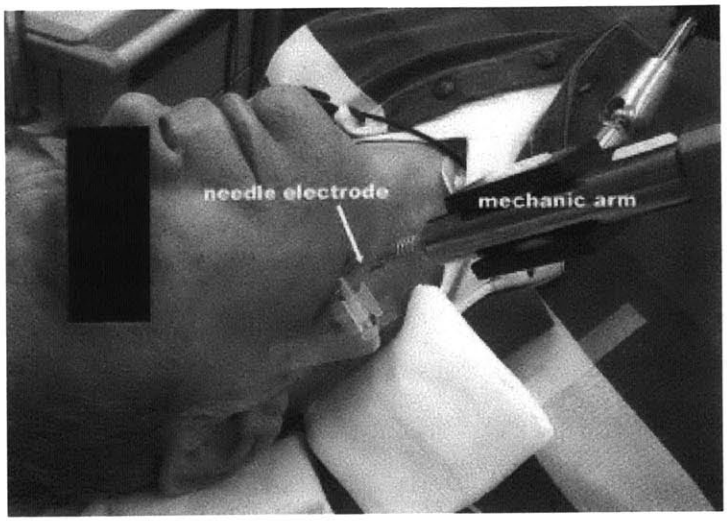

Figure 2.1 Use of polarographic electrode with mechanic arm in a cancer patient.

Vaupel et al. have studied the oxygenation of human tumors using computerized oxygen tension measurements based on the Eppendorf polarographic electrode. They obtained direct oxygen partial pressure measurements in breast cancers and normal breast tissues. Oxygen partial pressure values in normal breast were consistent with oxygenation status of normal tissues and were significantly higher compared to those in breast cancers that were hypoxic [14]. Movsas et al. have performed a similar study in which they have used the Eppendorf oxygen microelectrode to characterize the severity of hypoxia in human prostate carcinoma. They compared measurements from a pathologically involved region of prostate to normal muscle and found that oxygen measurements from the cancerous prostate were significantly lower than those from normal muscle [15]. Gatenby et al. have used the same Eppendorf oxygen electrode to study the effect of radiation therapy on the oxygen distribution in squamous cell carcinomas of the head and neck. A needle electrode was passed through each tumor under computed tomography (CT) guidance. They reported increases in tumor oxygen tension for patients that responded completely to radiotherapy and deduced that oxygen plays a significant role in human tumor response to radiotherapy [16].

(ii) Compartment Syndrome

The Five P's constitute the classic signs and symptoms of compartment syndrome and are as follows [17]:

1) Pain: Pain in one of the major compartments attributed to compartment syndrome is one of the most common signs of compartment syndrome and is intensified with movement or application of pressure.
2) Paresthesia: This is the feeling of a tingling sensation or numbness. There is a loss of sensation below the compartment syndrome affected area.
3) Passive stretch: Muscles in the affected compartment experience immense pain upon stretching.
4) Pressure: There is appreciable rigidity in the affected compartment.
5) Pulselessness: Local microvasculature is affected due to compartment syndrome which results in loss of pulse.

These five signs however manifest themselves during an established compartment syndrome by which stage it may be too late to perform successful fasciotomy (the preferred surgical technique to treat compartment syndrome where the fascia is cut open to reduce intracompartmental pressure). This is why a compartment pressure measurement is used to confirm the initial diagnosis using the 5 P's and patient history, providing a more objective diagnosis [18]. The two most commonly used techniques for tissue pressure measurements in compartment syndrome are the Whitesides infusion technique and the Stryker device [19]. The Whitesides infusion technique consists of a mercury manometer, two plastic intravenous extension tubes, two 18 gauge needles, a 20 mL syringe attached to a 3-way stopcock, and a bottle of saline. The Stryker device is based on the same principle as the Whitesides infusion technique but compared to the latter it is more compact, portable, and allows measurements to be read directly from the display on the device. Figure 2.2 shows a diagram of the apparatus of the Whitesides infusion technique as well as a picture of the Stryker device used for making intracompartmental tissue pressure measurements.

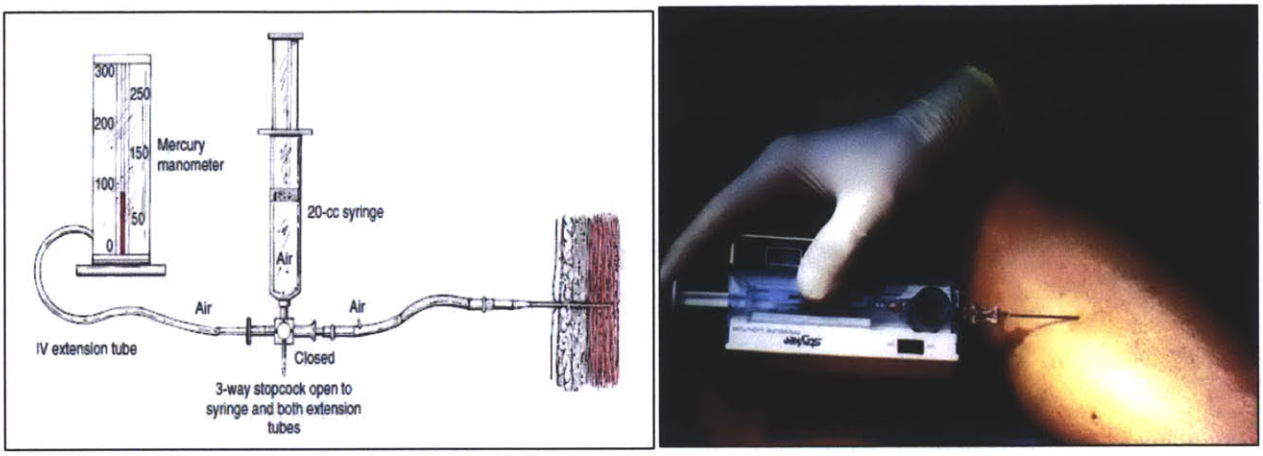

Figure 2.2 Clinical instrumentation used for diagnosing compartment syndrome in patients. Shown is the apparatus for Whitesides infusion technique (left) and the Stryker device (right).

Mohler et al. have studied the intramuscular pressure and relative oxygenation in the anterior compartment of the leg in patients suspected of having chronic compartment syndrome before, during and after exercise. They used an infusion-based technique for measuring intramuscular pressure and obtained oxygenation values using near infrared spectrometry. In their study they concluded that patients with chronic compartment syndrome (as confirmed by intramuscular pressure measurements) had greater relative deoxygenation during exercise as well as delayed reoxygenation after exercise and as such oxygenation measurements may be useful in diagnosing patients suspected of having chronic anterior compartment syndrome of the leg [20]. Seekamp et al. have used catheter-based measurements to study the effects of restricting blood circulation to the limbs of rats on the oxygen tension and intracompartmental pressure of the limb. They also conclude that intramuscular oxygen tension measurements could be a useful metric in diagnosing compartment syndrome especially in cases where there are normal compartment pressures [7].

Even though the abovementioned instrumentation and techniques used for measuring tumor oxygenation and intracompartmental pressure are widely used in clinical practice, they have their own limitations. First and foremost is the fact that they are extremely invasive procedures requiring injection of an electrode or needle each time a measurement needs to be made (which may be many times over the course of disease progression or therapy). This leads to patient discomfort and also implies that the measurements made are not repeatable as it is highly likely

that a specific site may not be examined each time the procedure is performed. One of the limitations specific to the polarographic oxygen electrode is that it is susceptible to pressure artifacts and the signal-to-noise ratio is very poor at low oxygen levels [12]. Similarly for intracompartmental measurements, Uliasz et al. have shown that the Whitesides infusion technique is not a reliable method for measuring intracompartmental pressure [21].

The impact of *in vivo* oxygen measurements on clinical practice and the limitations of current gold standards have encouraged researchers to develop alternative methods to detect oxygen *in vivo*. Some of these methods as well as their advantages and limitations are discussed in the next section.

2.2 Other methods to measure oxygen *in vivo* reported in literature

The use of nuclear medicine markers in conjunction with biopsy is one of the more invasive methods by which tumor hypoxia has been quantified by Chapman et al. Markers of the iodinated azomycin nucleoside class were used to test hypoxic activity in cell suspension equilibrated with different oxygen concentrations as well in tumor bearing rats [22]. Apart from being invasive this method does not yield a direct measurement of oxygen concentration but indicates hypoxia and is a predictor for tumor radioresistance.

Jiang et al. have used a fluorescence quenching based approach to quantify oxygen measurements *in vitro* and *in vivo*. They synthesized an oxygen-sensitive fluorescence indicator that was then attached to the distal end of a fiber optic cable which was encased in a catheter tube. The *in vitro* response of the sensor was characterized by exposing it to solutions infused with varying oxygen concentrations in a circulating loop system. *In vivo* measurements were performed by inserting the sensor into a collateral circulation system from the carotid artery of rabbits [23]. This sensor is reversible and has a fast response time of 15 s but involves an invasive procedure for measurements and is not repeatable. Xiong et al. have also reported the development of a dissolved oxygen sensor based on dynamic fluorescence quenching. The sensor was fabricated by dip-coating a silica-Ni-P coating onto a copper-screen substrate which

was then doped with an oxygen sensitive ruthenium complex. *In vitro* tests were carried out by introducing nitrogen-oxygen mixtures varying from 0% to 100% oxygen (v/v) into a flow-through cell containing water and the sensor [24]. Signal changes were reversible with response times of around 200-300 seconds. Although *in vivo* studies were not performed, it is conceivable that this approach would also require an invasive procedure for measurements that would not be repeatable.

Phosphorescence imaging is another technique that has been employed to detect *in vivo* oxygen concentrations. Wilson et al. have used a Pd complex-based phosphorescence probe infused into the femoral artery of a cat as a complex with bovine serum albumin. The response of the probe to occlusion and reperfusion of the middle cerebral artery is recorded using a video camera. This technique allows noninvasive measurements for detecting oxygen but is more of a surface detection scheme limited to depths of less than 1 mm [25]. Babilas et al. have shown oxygen dependent phosphorescence quenching using transparent planar sensor foils. The sensors consisted of a Pt complex immobilized in a polystyrene matrix that was spread onto a polyester support. Transcutaneous pO_2 measurements were taken before, during and after ischemia that was established using a tourniquet positioned on the upper arm of human subjects [26].

Professor Harold Swartz of Dartmouth Medical School has pioneered the use of electron paramagnetic resonance (EPR) spectroscopy for tissue oximetry. Williams et al. have recently reported on the use of India ink for EPR oximetry. Ongoing studies include those on human subjects for the measurement of subcutaneous pO_2 in the feet to assist in developing procedures for the treatment of peripheral vascular disease as well as tumor oximtery [27]. The technique involves injection of an oxygen sensitive dye, i.e. India ink, into the tissue of interest that can be read using a noninvasive and repeatable procedure. EPR spectroscopy is a promising technique for tissue oximetry but it is not used as MRI or NMR methods in clinical practice.

Magnetic Resonance Imaging (MRI) based methods have been used in the past to study tissue hypoxia and tumor oxygenation. These methods have primarily focused on the use of oxygen sensitive contrast agents such as hexafluorobenzene whose T_1 relaxation (discussed in Chapter 3) changes with oxygen and can be read using ^{19}F MRI [28]. The method involves injection of the

contrast agent in the tissue of interest and allows for noninvasive and repeatable measurements. The varying clearance rates of these compounds could be a potential concern especially for longer term studies.

Chapter 3: Magnetic Resonance (MR) Theory

This chapter provides a basic overview of the magnetic resonance phenomenon from a classical perspective, although a detailed understanding requires a quantum mechanical approach. The chapter begins by discussing nuclear spins and how they are manipulated in the presence of a main magnetic field B_o with a radiofrequency excitation field B_1 to generate relaxation of magnetic spins. The chapter closes by describing two basic pulse sequences, saturation recovery (SR) and inversion recovery (IR), that have been used in the experiments detailed in subsequent chapters.

3.1 Nuclear spins and the main field B_o

The phenomenon of magnetic resonance pertains to atoms with an odd number of nucleons (protons and/or neutrons) possessing a nuclear spin angular momentum. A nucleus has a net positive charge and can be thought of as spinning about its axis. The nucleus thus acts as a small magnet along the direction of the spinning axis (Figure 3.1). Hydrogen or ^{1}H with a lone proton is the most abundant atom with nuclear spin in the human body and is what most of MR imaging is catered to (including our own studies) although other atoms such as carbon (^{13}C), fluorine (^{19}F) and phosphorous (^{31}P) have also been imaged using MRI [28], [29], [30].

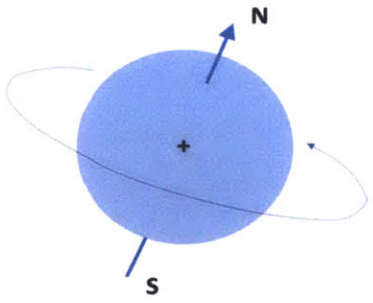

Figure 3.1 Nuclei with an odd number of nucleons are constantly spinning and can be thought of as tiny magnets possessing nuclear spin angular momentum.

The earth's magnetic field is too weak (approximately 5 G) and has practically no influence on these atomic or molecular 'spins'. This implies that in the absence of an external magnetic field the spins in a sample of material are oriented randomly with no preferential direction leading to zero net magnetization. In the presence of an externally applied static magnetic field B_o, however, most spins will align parallel to the direction of the magnetic field resulting in a non-zero net magnetization (Figure 3.2). The main field B_o also has the effect of causing the nuclear spins to precess at a specific frequency called the Larmor frequency. The Larmor frequency varies with the type of atom as well as the strength of the main magnetic field as shown by the equation,

$$\omega_o = \gamma B_o \tag{3.1}$$

which can also be written as

$$f_o = \frac{\gamma}{2\pi} B_o \tag{3.2}$$

where ω_o or f_o is the Larmor frequency, γ is the gyromagnetic ratio that is a constant different for each atom, and B_o is the main magnetic field.

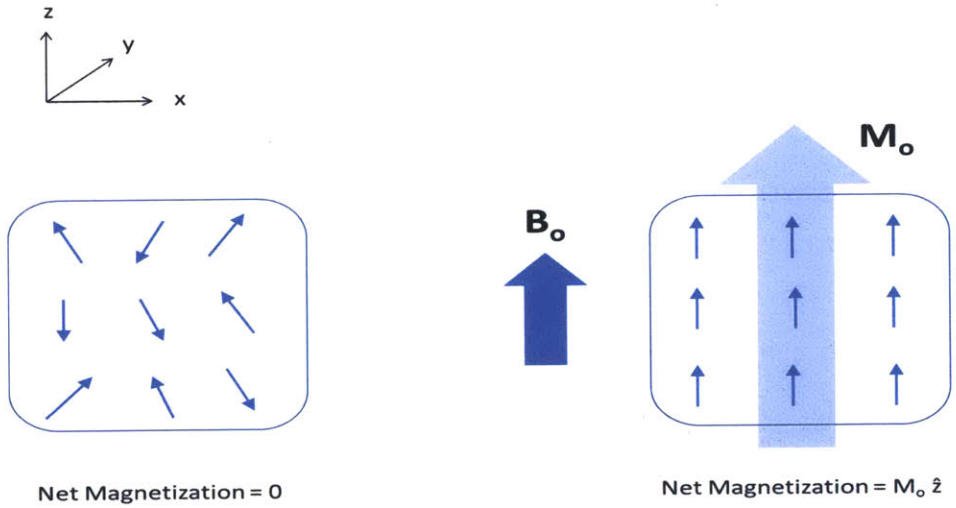

Figure 3.2 A sample consists of randomly pointing nuclear spins with zero net magnetization in the absence of a magnetic field. In the presence of an external field B_o, however, these spins align themselves along the direction of the applied field generating a net magnetization in the same direction.

3.2 MR excitation using an RF field B_1

The nuclear spins orient themselves parallel to the main field B_o which is the lower energy state. A subset of the spin population can also orient itself anti-parallel to B_o which is the higher energy state. The relative distribution of nuclear spins in these two energy states in the absence of the excitation field B_1 is described by the Boltzmann equation,

$$\frac{N_{anti-parallel}}{N_{parallel}} = e^{-\frac{\Delta E}{kT}} = e^{-\frac{h\gamma B_o}{2\pi kT}} \tag{3.3}$$

where $N_{parallel}$ is the number of nuclei in the lower energy state, $N_{anti\text{-}parallel}$ is the number of nuclei in the higher energy state, ΔE is the difference in energy levels of the two populations, γ is the gyromagnetic ratio, B_o is the main magnetic field, k is the Boltzmann constant, and T is the absolute temperature. Under equilibrium conditions and at room temperature this ratio is slightly less than 1 implying that there is a small excess of spins in the parallel or low energy state. It is the presence of these spins that gives rise to the net magnetization parallel to B_o.

These spins need to be perturbed from equilibrium in order to obtain an MR signal. This is achieved by using an RF pulse which generates a magnetic field B_1 in the transverse (xy) plane and is perpendicular to the main field B_o which points in the longitudinal or z direction. The RF pulse must be operating at the resonant frequency of the spins, i.e., the Larmor frequency ω_o in order to excite the nuclear spins. Excitation can be thought of as rotating the magnetization vector M_o into the transverse plane as it precesses about the longitudinal axis at the Larmor frequency (Figure 3.3). The magnetization vector does not necessarily have to be tipped 90° into the transverse plane. It can be tipped about by some arbitrary angle which depends on the strength and duration of the RF pulse B_1.

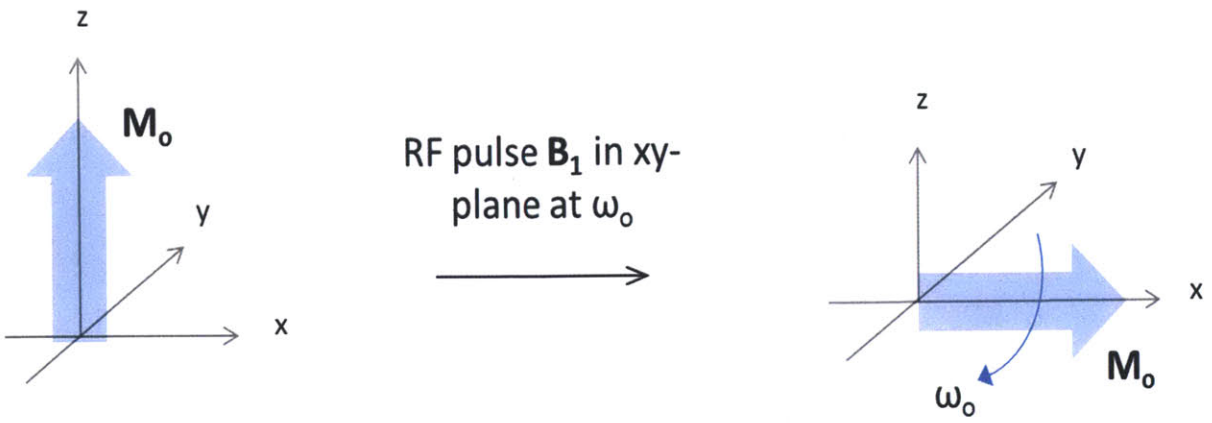

Figure 3.3 Excitation of spins is achieved using an RF pulse that generates a magnetic field B_1 in the transverse plane. The magnetization vector is tipped about by a certain angle (90° in the figure shown).

The RF pulse essentially provides the energy separating the two spin populations causing a transition of spins between the two states. It is in this excited state that a signal called the free induction decay (FID) can be picked up in the transverse plane.

3.3 MR relaxation

The spins or more specifically the net magnetization will eventually return to the initial thermal equilibrium state through a process called MR relaxation. The transverse component of magnetization (M_{xy}) decays to zero whereas the longitudinal component (M_z) reaches the equilibrium magnetization M_o. Figure 3.4 shows these relaxation processes in terms of the net magnetization vector.

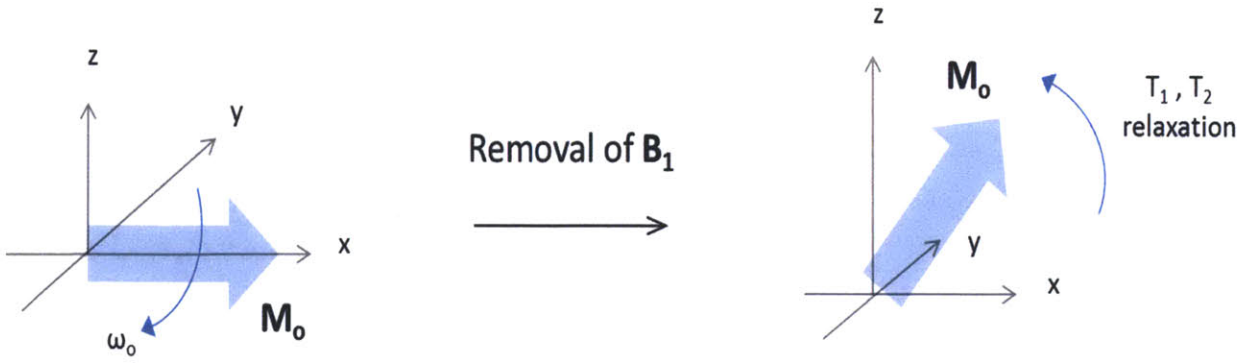

Figure 3.4 The nuclear spins return to thermal equilibrium once the RF pulse B_1 is terminated. As shown in the above figure, the transverse or xy component of the magnetization vector decays from *Mo* to zero while the longitudinal or z component increases from 0 to M_o.

The longitudinal relaxation is characterized by the time constant T_1 which is also known as the spin-lattice time constant. Recovery of the longitudinal component of magnetization is described by

$$\frac{dM_z}{dt} = -\frac{M_z - M_o}{T_1} \tag{3.4}$$

the solution of which is

$$M_z = M_o + (M_z(0) - M_o)e^{-\frac{t}{T_1}} \tag{3.5}$$

where $M_z(0) = M_o$ for a 90° excitation.

The time constant characterizing the decay of the transverse component of magnetization is referred to as T_2 which is also called the spin-spin time constant. It is described by

$$\frac{dM_{xy}}{dt} = -\frac{M_{xy}}{T_2} \tag{3.6}$$

whose solution is

$$M_{xy} = M_{xy}(0)e^{-\frac{t}{T_2}} \tag{3.7}$$

where $M_{xy}(0) = M_o$ for a 90° excitation.

3.4 Basic pulse sequences for T_1 measurement

The material synthesized and presented in this thesis for use as an implantable oxygen sensor has a T_1 that is dependent on the partial pressure of oxygen. Thus, oxygen tension determination for *in vitro* characterization as well as for *in vivo* measurements requires extraction of the T_1 time constant of the material. This section describes two pulse sequences that have been used in our work.

(i) Saturation Recovery

The saturation recovery sequence is composed of a series of 90° pulses. These pulses are separated by a repetition time denoted by *TR*. The effect of the 90° pulse is to flip the magnetization vector into the transverse plane such that the longitudinal component of magnetization is 'saturated' to zero. The magnetization recovers exponentially to the equilibrium magnetization M_o with a time constant of T_1 after the pulse is applied. Figure 3.5 shows a basic saturation recovery sequence. The image intensity is proportional to the longitudinal magnetization, M_z, right before the application of the second 90° pulse when steady-state is achieved, i.e.,

$$I \propto M_z = M_o(1 - e^{-\frac{TR}{T_1}}) \tag{3.8}$$

where I is image intensity.

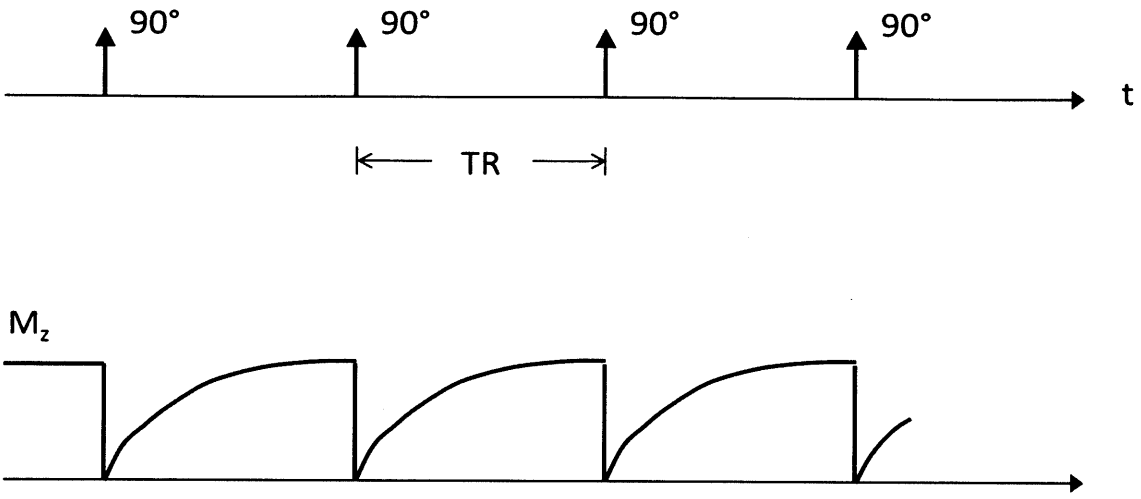

Figure 3.5 A basic saturation recovery sequence comprising of a series of 90° pulses separated by *TR*. Longitudinal magnetization goes to zero upon application of the pulse and followed by T_1 relaxation.

(ii) Inversion Recovery

The inversion recovery sequence is so named because it consists of an initial 180° pulse that inverts the initial magnetization. The longitudinal magnetization relaxes with time constant T_1 until a 90° pulse is applied after a time delay of *TI*. This 90° pulse forces the longitudinal magnetization to zero after which it recovers once again following T_1 relaxation until another 180° pulse is applied a time delay of *TR* after the first 180° pulse, and so on. Figure 3.6 depicts this scheme. The image intensity is proportional to the longitudinal magnetization, M_z, right before the application of the second 90° pulse when steady-state is achieved, i.e.,

$$I \propto M_z = M_o(1 - 2e^{-\frac{TI}{T_1}} + e^{-\frac{TR}{T_1}}) \tag{3.9}$$

where I is the image intensity.

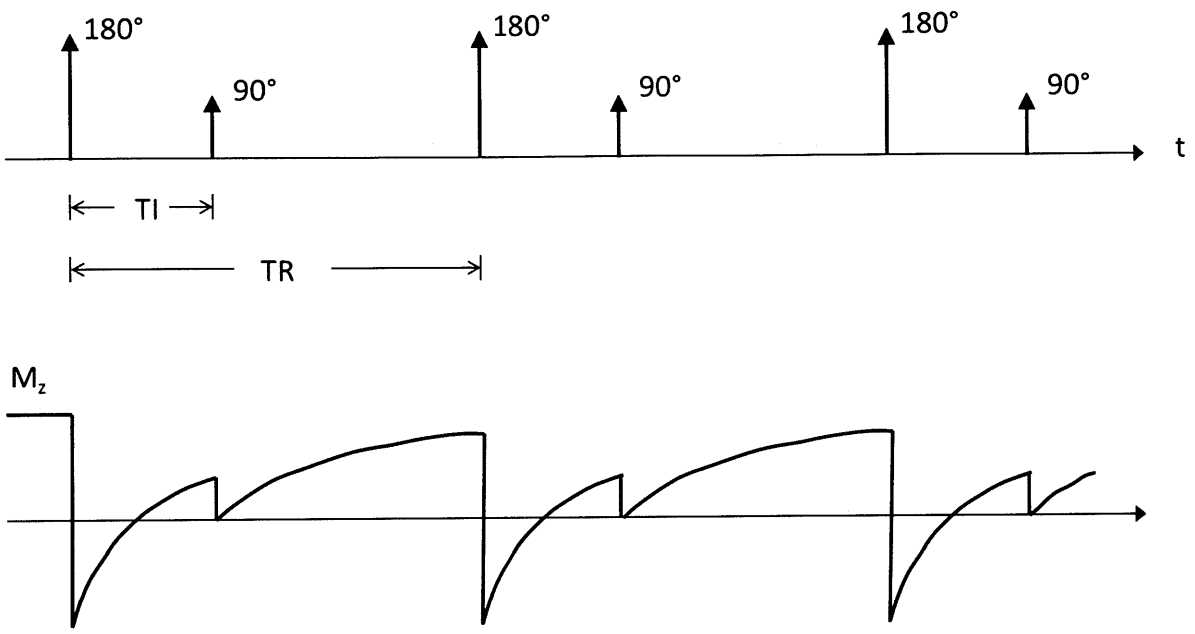

Figure 3.6 A basic inversion recovery sequence and the corresponding time course of longitudinal magnetization.

Chapter 4: Synthesis and *in vitro* Characterization

4.1 DDMPS as the oxygen sensing component

Dodecamethylpentasiloxane (DDMPS) was selected as the material of choice due to its sensitivity to oxygen and corresponding MR-responsiveness. DDMPS is a linear siloxane molecule and belongs to the larger family of organosilicon compounds. It is a colorless liquid at room temperature with low viscosity and consists of a linear chain of five silicon atoms bonded together with oxygen atoms between them (Figure 4.1). It is the fifth in the series of linear siloxane molecules after hexamethyldisiloxane (HMDSO), octamethyltrisiloxane (OMTSO) and decamethyltetrasiloxane (DMTSO), in order of increasing number of silicon (and oxygen) atoms. DDMPS and DDMPS-derived materials have been used in products such as antiperspirants, deodorants, lotions, cosmetics etc. and as such are biocompatible [31].

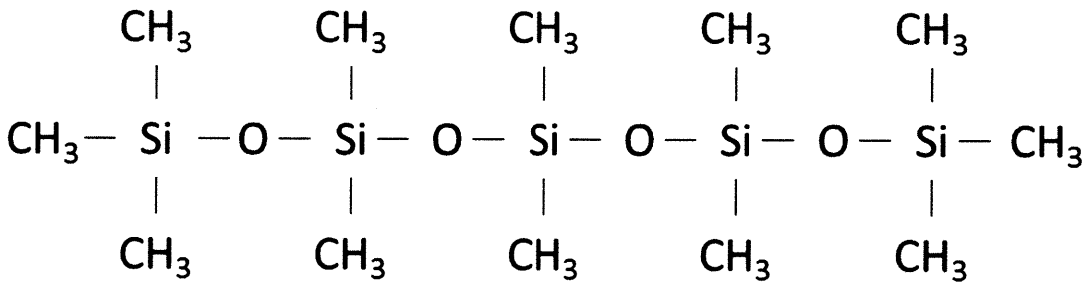

Figure 4.1 Molecular structure of dodecamethylpentasiloxane (DDMPS).

DDMPS is sensitive to oxygen in that its longitudinal relaxation time constant T_1 varies with oxygen percentage. Figure 4.2 shows the variation in T_1 with time as DDMPS is exposed to a nitrogen/oxygen mixture of gas with varying percentages of oxygen. T_1 measurements were made using the Bruker Minispec which is a 0.47 T benchtop relaxometer manufactured by the Bruker Corporation. 1-2 mL of DDMPS (97%, Sigma-Aldrich) was pipetted into a 10 mm NMR tube (Norell, Inc.) and placed into the Bruker Minispec magnet. The sample was allowed to equilibrate to the magnet temperature of 40°C for few minutes before T_1 measurements were made spaced 1 min apart. A two-gas gas mixer (Columbus Instruments) was used to

electronically set and control the gas composition that was fed into the head space over the DDMPS in the NMR tube at a flow rate of 50 cc/min.

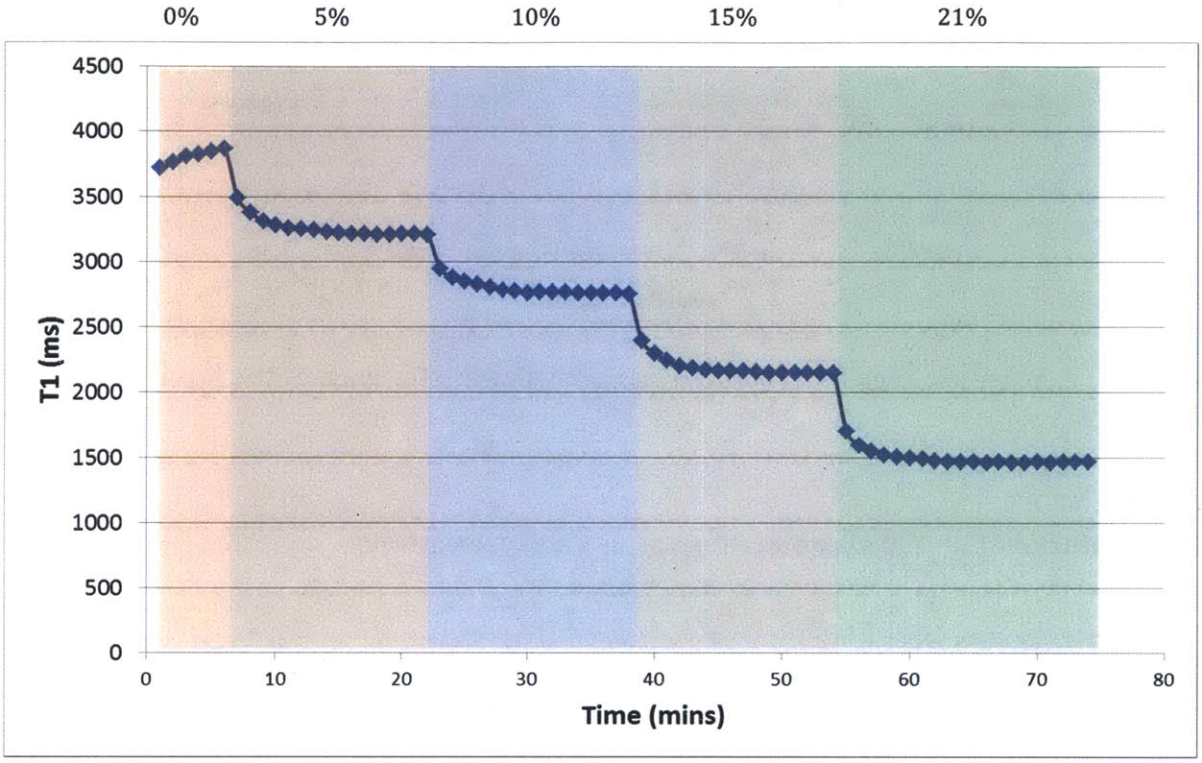

Figure 4.2 Time course measurements of T_1 with varying percentage of oxygen in a nitrogen/oxygen gas mixture for DDMPS. 0% oxygen implies 100% nitrogen.

These results suggest a response time of around a minute and an equilibration time of around 5 minutes. The equilibration time will vary, however, depending on several factors other than the material itself such as amount of sample, gas flow rate etc. It is pertinent to mention here why DDMPS and not any of the other linear siloxanes HMDSO, OMTSO or DMTSO were considered for use as the oxygen sensing component. Although HMDSO, OMTSO and DMTSO show a larger dynamic range or % change in T_1 from 21% to 0% oxygen (see Chapter 5), the fact that these siloxanes are more volatile than DDMPS makes the selection of the latter worth the tradeoff. Figure 4.3 below shows the T_1 sensitivity (measured as the % change in T_1 between 0% and 21% O_2) versus volatility (measured by the evaporation rate of each liquid siloxane in an open vial at 37°C).

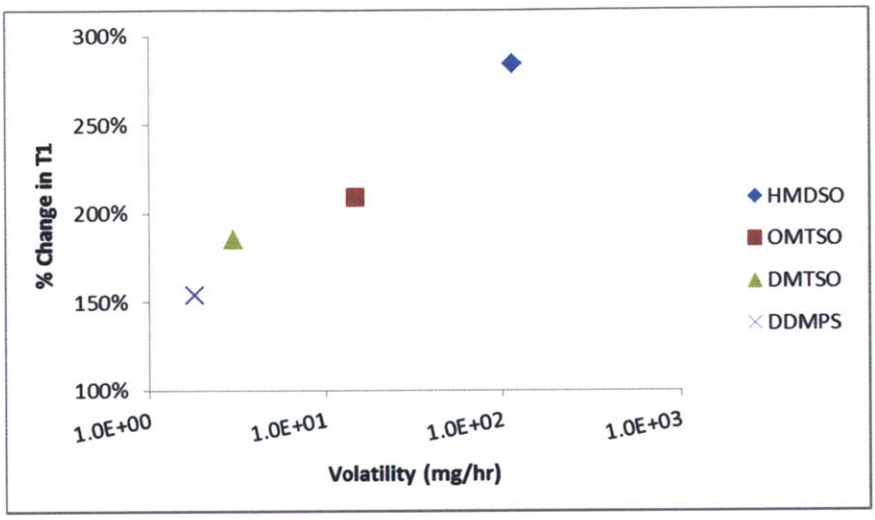

Figure 4.3 T_1 response sensitivity plotted against volatility for each of the liquid siloxanes.

4.2 Synthesis of a solid elastomer for use as an oxygen sensor

The use of liquid DDMPS alone for reporting tissue oxygenation *in vivo*, though possible, has its limitations. Clearance with time of the injected liquid, or its emulsion, and the failure to accurately monitor a specific site repeatedly due to potential perfusion of the liquid in tissue are but some of the reasons why using liquid DDMPS may not be beneficial. One way to address this is to enclose DDMPS within a biocompatible plastic reservoir using an oxygen permeable membrane, based on an approach used by Ling et al. to detect cardiac biomarkers *in vivo* [32]. Although this approach is possible, a standalone polymer that could be molded into different shapes and sizes is a more attractive proposition.

A standalone polymer with DDMPS in a polydimethylsiloxane (PDMS) network was synthesized to address the aforementioned limitations, where the former is the oxygen sensitive component and the latter provides structural integrity. PDMS belongs to the family of organosilicon compounds commonly known as silicones. Figure 4.4 shows the molecular structure of PDMS which consists of n repeating units of $[SiO(CH_3)_2]$.

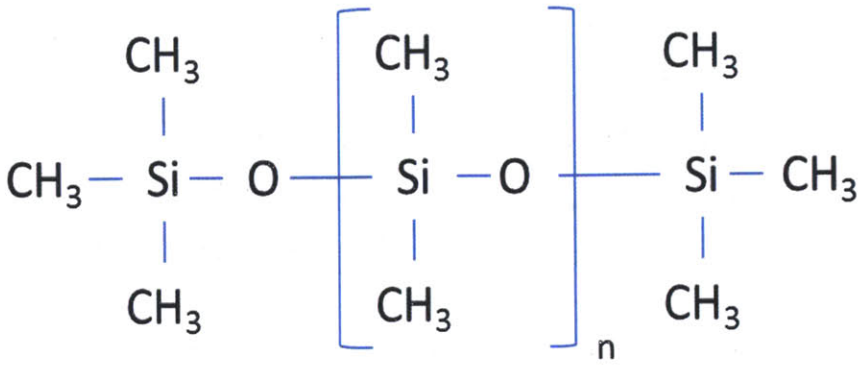

Figure 4.4 Molecular structure of polydimethylsiloxane (PDMS).

PDMS is a transparent, non-toxic, biocompatible and biodurable elastomer that has been used extensively for various biomedical applications. It has been used, for example, in blood-oxygenator membranes, shunts, catheters, hand and foot joint implants, breast implants and testicular implants among other applications [33]. Silicones like PDMS are also known to have a high permeability to oxygen which is a key requirement for our application since this ensures rapid response and equilibration times (see Chapter 5).

Synthesis of the oxygen sensitive solid elastomer is accomplished by mixing 70% by weight of DDMPS (97%, Sigma-Aldrich) and 30% by weight of PDMS (Sylgard 184, Dow Corning). The two components were vigorously mixed in a vial until the PDMS completely dissolved resulting in a clear liquid. This was possible due to the miscibility of DDMPS in uncured PDMS given that both belong to the same class of materials, i.e., siloxanes. The PDMS portion of this mixture comprised of a 10:1 w/w ratio of base to curing agent. The DDMPS-PDMS mixture was poured into a plastic petri dish that was coated with a thin film of Teflon to allow for release of the elastomer once cured. This small petri dish was then placed in a larger plastic petri dish that also contained a small aluminum weighing boat filled with pure DDMPS (Figure 4.5). The DDMPS filled boat was used to ensure a vapor saturated environment in the large petri dish so as to prevent any loss of DDMPS from the 70% DDMPS / 30% PDMS mixture inside the smaller petri dish during thermal cure. The large petri dish and its contents were then transferred to a lab oven maintained at 80°C and cured for 1.5 hrs.

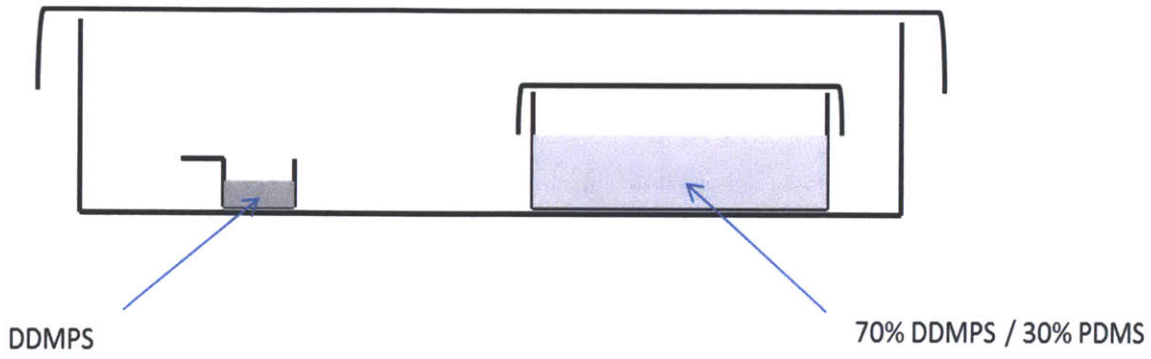

Figure 4.5 Petri dish setup for curing elastomer while ensuring vapor saturated conditions at the same time.

A soft, transparent and elastomeric mold was retrieved upon completion of thermal curing. This solid elastomeric material will be referred to as 70% DDMPS-PDMS. Weight measurements taken before and after thermal cure were the same verifying that no loss of DDMPS had occurred and that the vapor saturation scheme was indeed effective. The synthesis process for 70% DDMPS-PDMS makes it possible to synthesize sensors of various shapes and sizes as may be required for particular implantation site. This can be achieved by using appropriate Teflon molds. Figure 4.6 below shows a large disc of 70% DDMPS-PDMS that was prepared in a petri dish and smaller disc-shaped devices that were punched out from this larger disc. Devices of different sizes were obtained using biopsy punches (KAI Medical) of various diameters.

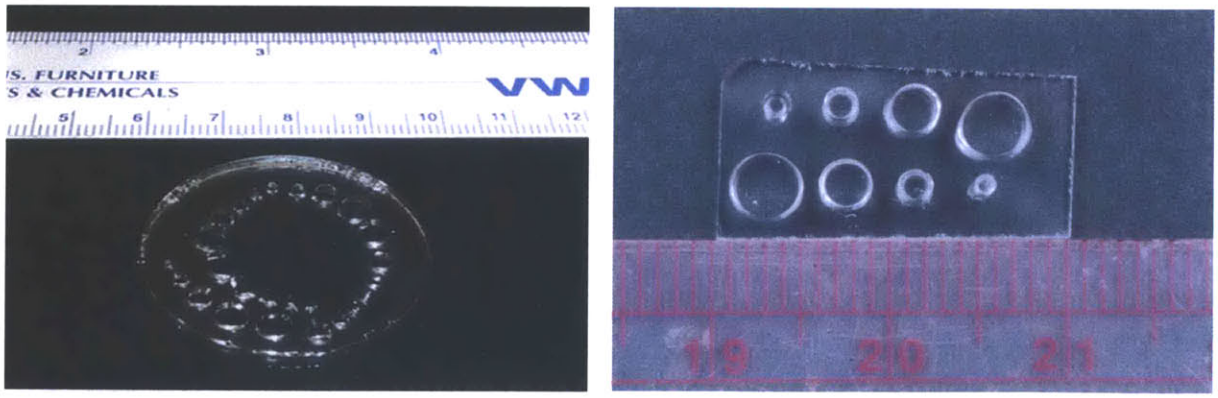

Figure 4.6 70% DDMPS-PDMS mold prepared using the synthesis protocol outlined earlier (left) and devices with diameters ranging from 1-4 mm punched out from the larger mold (right).

4.3 Response of the solid elastomer to oxygen

The response of 70% DDMPS-PDMS to oxygen was measured using the same instruments and setup used for measuring the response of pure DDMPS (see Section 4.1). Three discs were punched out from a mold of 70% DDMPS-PDMS using a 4 mm biopsy punch. These discs were placed in a 10 mm NMR tube which was then placed inside the Minispec magnet and allowed to equilibrate to the magnet temperature of 40°C for few minutes before T_1 measurements were made spaced 10 min apart. An initial measurement was taken under ambient conditions (air or 21% oxygen) and then the devices were exposed to 0%, 5%, 10%, 15% and 21% oxygen in that order. The devices were exposed to different oxygen concentrations by using a nitrogen/oxygen gas mixer system with the output of the gas mixture set to a flow rate of 50 cc/min. Figure 4.7 shows a plot of the device response as it was exposed to a mixture of nitrogen and oxygen gases with varying oxygen concentrations.

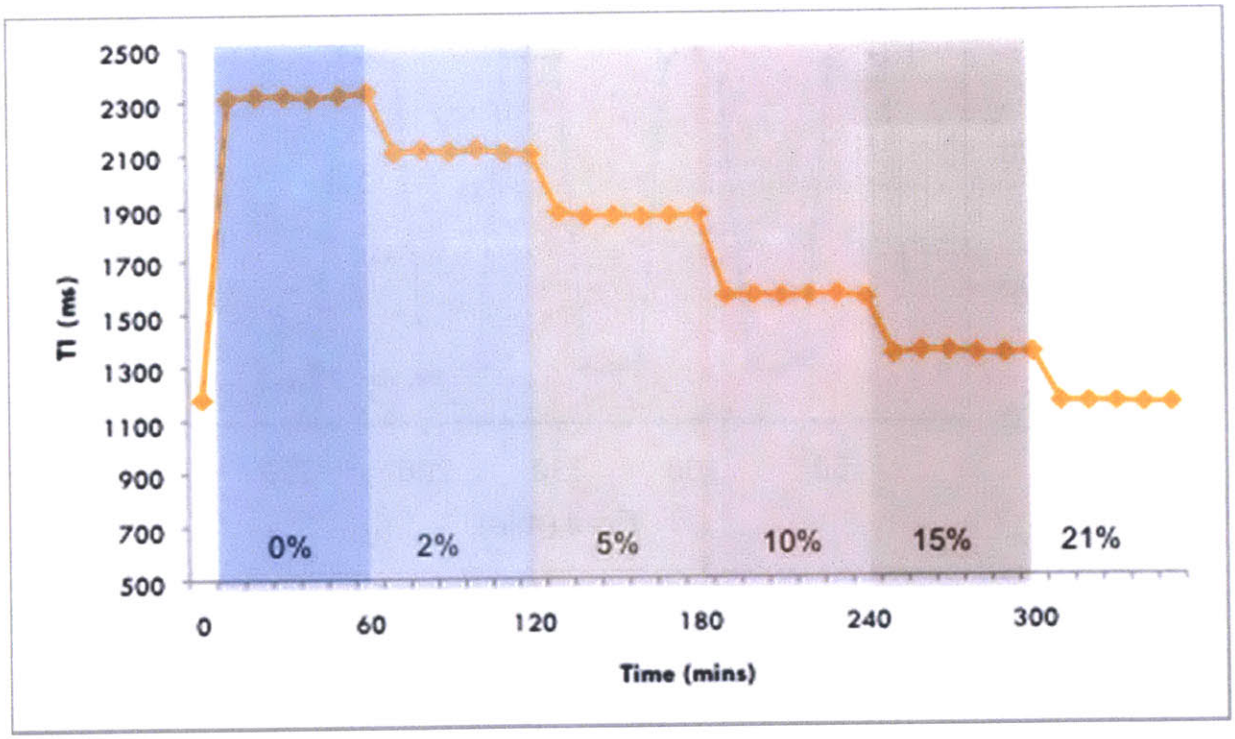

Figure 4.7 T_1 response of 70% DDMPS-PDMS devices tracked over time for different oxygen concentrations. % values indicate the oxygen concentration the devices were exposed to during that period. 0% oxygen implies 100% nitrogen.

Measurements were found to be stable for each interval of specific oxygen concentration. The device response equilibrated within 10 minutes which suggests a response time of well under 10 minutes. Separate measurements showed the response time to be around a minute and an equilibration time of 6 minutes. As mentioned previously, the equilibration time will vary depending on factors other than the material itself such as gas flow rate, size of device etc. This does not, however, mean that the value of this metric is meaningless since it gives an order of magnitude sense for the response and equilibration times of the material. The response was found to be completely reversible as established by cycling the gas mixture between 0% and 21% oxygen levels several times (Figure 4.8). T_1 measurements for different oxygen concentrations were used to generate a calibration curve correlating the longitudinal relaxation rate, $1/T_1$, to the oxygen concentration, % O_2 (Figure 4.9). This calibration curve can be used to extrapolate oxygen concentration for a given T_1 measurement of the device at 0.47 T.

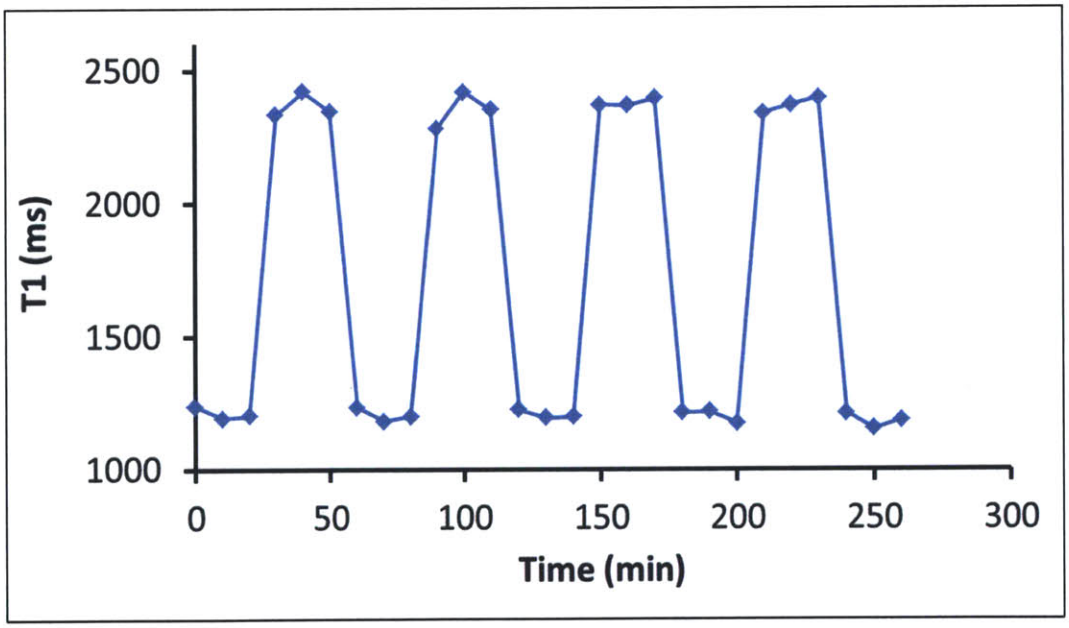

Figure 4.8 Reversibility of response for 70% DDMPS-PDMS. Gas was cycled between 0% oxygen (top plateau) and 21% oxygen (bottom plateau) showing complete reversibility.

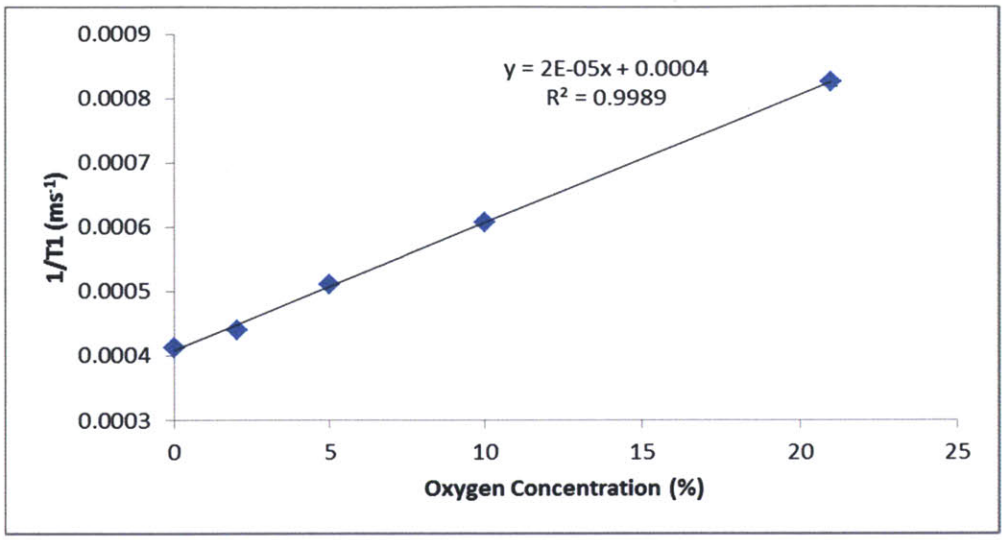

Figure 4.9 Calibration curve for 70% DDMPS-PDMS using the Minispec at 0.47 T.

Regression analysis was performed on the calibration curve using Excel to determine: (i) the limit of detection (LOD) which was found to be 1.06% O_2; and (ii) the limit of quantification (LOQ) which was calculated to be 3.21% O_2. It is pertinent to mention here that the physiologically relevant oxygen levels are 0-4% (hypoxic tissue), 4-7% (venous blood), 7-12% (regular tissue) and 12-20% (arterial blood). The 70% DDMPS-PDMS sensors show response in all these ranges and with a lower LOQ of around 3% can also detect hypoxic tissue.

4.4 Specificity of response to oxygen

It is important to ascertain that the response of the device has high specificity to oxygen, i.e., it does not respond to other gases. This is because any response attributable to some gas other than oxygen can lead to false readings and spurious extrapolation of the actual concentration of oxygen based on the recorded T_1 measurement. Oxygen and carbon dioxide are the two major gases present in blood and are of interest for blood gas measurements. Values at sea level for the partial pressure of oxygen, PaO_2, are in the range of 75-100 mmHg and those for carbon dioxide, $PaCO_2$, are in the range of 38-42 mmHg [34]. These partial pressure values roughly translate to 10-13% for oxygen and 5-5.5% for carbon dioxide given an atmospheric pressure of 760 mmHg at sea level.

A test for response of the devices to carbon dioxide was performed by preparing disc shaped devices and exposing them to CO_2. Three disc shaped devices were punched out from a mold of 70% DDMPS-PDMS using a 4 mm biopsy punch and placed into a 10 mm NMR tube. The tube was placed in the Minispec magnet and allowed to equilibrate to the magnet temperature of 40°C for few minutes before T_1 measurements were taken. An initial measurement was taken under air followed by three measurements each at nitrogen (0% O_2 or 0% CO_2) and 100% carbon dioxide respectively. A gas mixer system was used to switch between nitrogen and carbon dioxide gases. Measurements were taken every 10 minutes. Figure 4.10 shows a bar chart comparing the initial measurement in air and the measurements taken at 0% and 100% carbon dioxide levels. The results clearly show that there is no significant difference in T_1 response of the 70% DDMPS-PDMS between 0% and 100% carbon dioxide levels. It can safely be assumed then that much lower carbon dioxide levels present *in vivo* as mentioned above will not affect the response of the device to oxygen either.

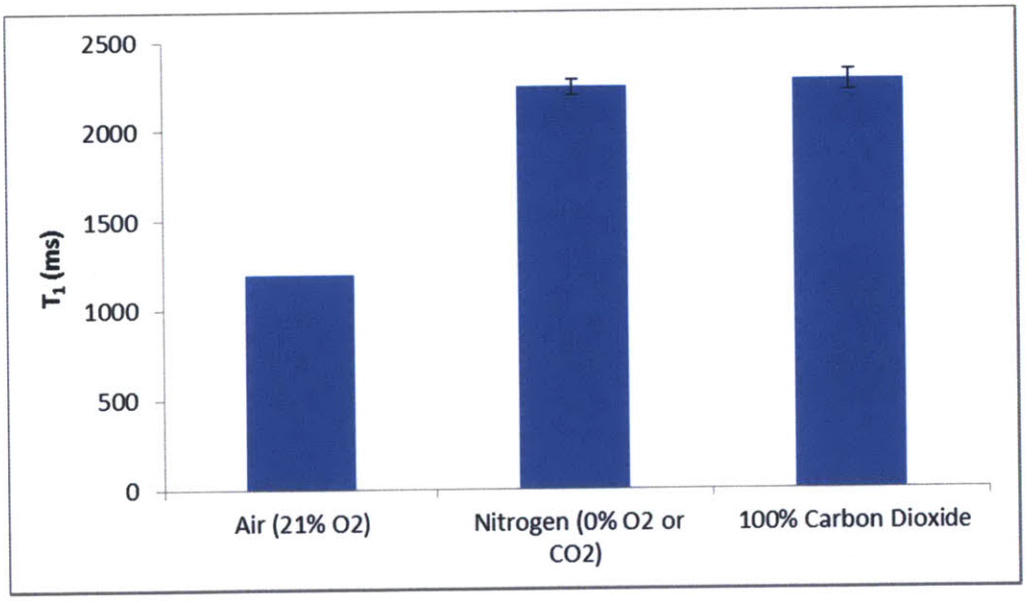

Figure 4.10 Comparison of the T_1 response of 70% DDMPS-PDMS when exposed to air (21% O_2), nitrogen (0% O_2 and 0% CO_2) and 100% CO_2 levels. The material responds to oxygen (Air vs. Nitrogen) whereas there is no response to CO_2 (Nitrogen vs. CO_2). This shows that 70% DDMPS-PDMS has a specific response to O_2.

Chapter 5: Oxygen Diffusivity Measurements

Oxygen is highly permeable in silicones and siloxanes, and is characterized by large permeabilities in these materials [35]. The polymer material synthesized and presented in this thesis for use as an injectable oxygen sensor is composed of a siloxane, dodecamethylpentasiloxane (DDMPS), within a polydimethylsiloxane (PDMS) matrix. DDMPS belongs to a family of linear siloxanes that also include hexamethyldisiloxane (HMDSO), octamethyltrisiloxane (OMTSO) and decamethyltetrasiloxane (DMTSO) among others. Table 5.1 shows the molecular structure and weight of each of these four linear siloxanes.

Siloxane	Molecular Structure	Mol. Wt. (g/mol)
HMDSO	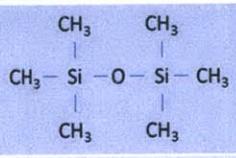	162.38
OMTSO	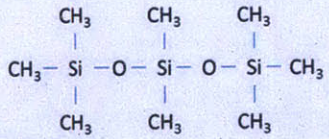	236.53
DMTSO	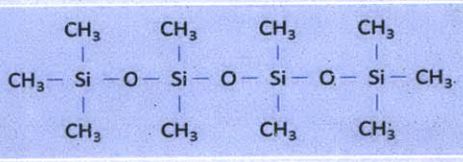	310.69
DDMPS	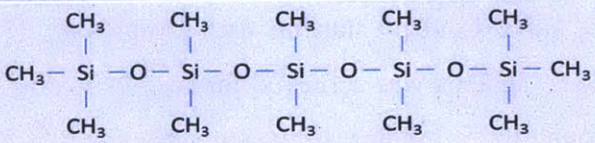	384.84

Table 5.1 Molecular structures and weights of the four linear siloxanes used for diffusivity measurements and analysis.

Oxygen diffusivity in the sensor materials is important to know not only to ascertain the response and equilibration times but also to explain the changes in T_1 observed in response to oxygen. We hypothesized that the diffusivity of oxygen in these materials dictates their sensitivity in T_1

response to oxygen, with higher oxygen diffusivities resulting in higher T_1 sensitivities and vice versa which was found to be the case (see section 5.2). This can be thought of as follows: an oxygen molecule moving in a material with higher oxygen diffusivity will cause a larger number of protons to relax compared to one moving in a material with lower oxygen diffusivity leading to the differences in T_1 sensitivities.

Oxygen diffusivity measurements were carried out in each of the four liquid siloxanes mentioned above as well as in the corresponding solid 70% Siloxane-PDMS composite blends. The measured diffusion coefficients were correlated with the percentage change in T_1 in response to oxygen so as to try to better understand the mechanisms behind the T_1 response of these materials. Various methods have been reported in literature in order to determine the diffusion coefficient of gases in polymers. Some of these include luminescence quenching [36], electron spin resonance [37], and sorption/desorption [38]. Our approach involved using MR intensity measurements for obtaining oxygen diffusivities. The (defined) variation in T_1 of these materials with oxygen was leveraged in order to track the change in intensity with time at a fixed depth upon exposing these materials to oxygen. The protocol for oxygen diffusion measurements is described in detail next.

5.1 Protocol for oxygen diffusivity measurements

(i) Equilibrating samples at 0% oxygen:

Diffusion experiments were carried out by starting with samples initially at 0% oxygen and by exposing them to air at time $t = 0$. This was achieved for liquid siloxane samples by purging gas-tight GC vials with lab nitrogen for 5 minutes. In the case of solid 70% Siloxane-PDMS samples, an uncured mixture prepared in gas-tight GC vials was purged with lab nitrogen for 5 minutes followed by thermal cure at 80°C for 1.5 hrs. The nitrogen gas used for purging the samples was vapor saturated with the respective liquid siloxane by bubbling through this siloxane in a cold finger to prevent loss of the 70% by weight siloxane component during the curing process. T_1 measurements were taken in the end to ensure that the samples were indeed equilibrated at 0% oxygen.

(ii) MR intensity time-course at a fixed depth:

A 1D intensity profile was taken for each sample before exposing it to air. This profile was used to determine the height of the column of sample in the gas-tight vial so as to set the sample at a known fixed depth for MR intensity measurements. The height of the column of sample was also necessary for fitting the time-course measurements to the diffusion equation as will be discussed later. The sample was profiled and set at a particular depth using a motion stage while MR intensity measurements were performed using a bench-top 0.43 T AutoNMR probe and a saturation recovery pulse sequence. Measurements were performed at 25°C. Figure 5.2 below shows this measurement setup.

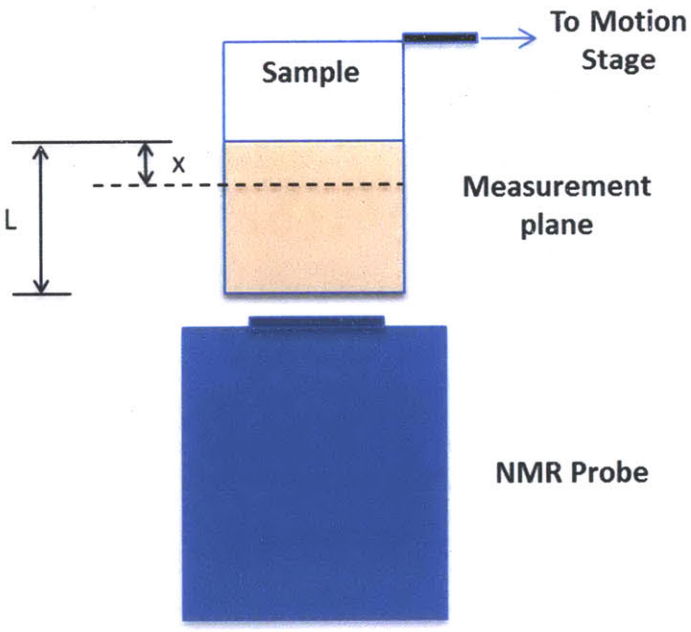

Figure 5.2 Setup for measuring oxygen diffusion. *L* is the length of the column of sample and *x* is the depth at which intensity measurements are taken.

Repetition times (*TR*) were chosen such that maximum contrast in intensity between 0% oxygen (initial state) and 21% oxygen (final state upon exposure to air) was achieved. This optimal *TR* was obtained by differentiating the difference in intensities between 0% and 21% oxygen with respect to *TR* and equating to zero, leading to the following equation for computing it,

$$TR_{opt} = \frac{\ln(\frac{T_{1|21}}{T_{1|0}})}{\frac{1}{T_{1|0}} - \frac{1}{T_{1|0}}} \quad (5.1)$$

where $T_{1|21}$ is the T_1 of the material at 21% oxygen and $T_{1|0}$ is the T_1 of the material at 0% oxygen.

(iii) Conversion of intensity measurements to % O_2:

The acquired time-course measurements were first converted from intensity to % O_2 (concentration) in order to extract oxygen diffusion coefficients for the various samples. Since MR intensity is related to T_1 by the saturation recovery equation and the inverse of T_1 is linearly related to % O_2, this conversion was easily made using the equations,

$$I = I_o(1 - e^{-\frac{TR}{T_1}}) \quad (5.2)$$

$$\frac{1}{T_1} = a + b(\%\ O_2) \quad (5.3)$$

where I_o is the equilibrium intensity approximated by measuring intensity at a high TR, while a and b are coefficients that were determined experimentally.

(iv) Fitting to diffusion equation:

Diffusion through an isotropic medium is characterized by Fick's second law of diffusion which is described by the following equation,

$$\frac{\partial C}{\partial t} = D\frac{\partial^2 C}{\partial x^2} \quad (5.4)$$

where x is distance, t is time, C is the concentration of the diffusing species and D is the diffusion coefficient.

The solution for this equation in the case of an infinitely long sample for which $C(x) = 0$ for $x < 0$ and $t = 0$ while $C(x) = C_o$ outside the sample for all $t \geq 0$ is given by the following equation [39],

$$C = C_o erfc(\frac{x}{2\sqrt{Dt}}) \tag{5.5}$$

where $erfc$ is the complementary error function. This equation implies that for Fickian diffusion the diffusion distance varies linearly with the square root of time, i.e., $x \propto \sqrt{t}$. Oxygen is diffusing through a finite sample in our setup and therefore Equation 5.5 does not hold. A finite sample implies a zero flux condition at the bottom of the vial. The solution for this case can be thought of as the combination of an image source (a distance L below the sample) as a result of a single reflection at the boundary, along with the real source (at $x = 0$) so as to achieve zero-flux at the bottom of the vial. This leads to the following equation,

$$C = C_o[erfc\left(\frac{x}{2\sqrt{Dt}}\right) + erfc\left(\frac{x + 2L}{2\sqrt{Dt}}\right)] \tag{5.6}$$

where L is the length of the sample as shown in Figure 5.2 earlier. The % O_2 vs. time data from the previous step was fitted to this equation to retrieve the diffusion coefficient D for each sample.

5.2 Results

Figures 5.3 shows the changes in MR intensity and percentage oxygen with time for the liquid siloxane samples hexamethyldisiloxane (HMDSO), octamethyltrisiloxane (OMTSO), decamethyltetrasiloxane (DMTSO) and dodecamethylpentasiloxane (DDMPS), as the samples were exposed to air from their initially equilibrated state of 0% oxygen. Measurements were performed at a depth of 2.5 mm from the surface of the sample for each of the four liquid siloxanes. The results suggest equilibration times on the order of several minutes at the specified depth for each of the samples, increasing from about 4 minutes in the case of HMDSO to around 10 minutes for DDMPS. This suggests a decrease in oxygen diffusivity as we go from HMDSO

to DDMPS as can also be deduced from Figure 5.7 where the initial rate of increase in percentage oxygen decreases from HMDSO to DDMPS. This is also verified by the extracted oxygen diffusivity values in Table 5.2.

Similar time-course measurements for MR intensity and percentage oxygen for the 70% Siloxane-PDMS solid elastomeric samples are shown in Figures 5.4 for HMDSO, OMTSO, DMTSO, and DDMPS as the siloxane component respectively. The changes were tracked for samples initially equilibrated at 0% oxygen that were exposed to air at time $t = 0$. Measurements were made at a depth of 1.5 mm from the surface of the sample for each of the four 70% Siloxane-PDMS materials. The equilibration times of these solid samples at the specified depth are easily on the order of several hours, in stark contrast to the liquid samples. The initial slopes of the percentage oxygen time-course plots suggest a decrease in diffusivity from 70% HMDSO-PDMS to 70% DDMPS-PDMS as is verified by the extracted oxygen diffusivity values in Table 5.2. A quick glance of this table also shows that the oxygen diffusivity values for the 70% Siloxane-PDMS solid samples are about an order of magnitude lower than those for liquid siloxane samples which explains the longer equilibration times for the solid samples. This is not surprising as the cross-linked PDMS network of the 70% Siloxane-PDMS composites is a barrier to the diffusion of oxygen therefore resulting in lower oxygen diffusivities and longer equilibration times. The diffusion coefficient of oxygen in these composite materials, however, is larger than that of bare PDMS as is shown in Table 5.2. The oxygen diffusivity in PDMS was determined using the same protocol as for the other samples.

Many polymers exhibit non-Fickian diffusion that cannot be described using Fick's law. Glassy polymers are one such example. Elastomeric rubber polymers, however, obey Fickian diffusion. This difference is due to the fact that rubber polymers respond instantaneously to changes in external conditions whereas glassy polymers do not, the latter showing time-dependent behavior [40]. To ensure Fickian diffusion of oxygen in our 70% Siloxane-PDMS elastomeric solid samples the diffusion distance was plotted against the square root of time. Such a plot if linear would confirm the Fickian behavior of diffusion. Figure 5.5 shows these plots for 70% Siloxane-PDMS samples for each siloxane HMDSO, OMTSO, DMTSO and DDMPS. The plots were indeed linear confirming that the diffusion of oxygen in these polymers follows Fickian

behavior. The line gradients of these plots decrease as we go from 70% HMDSO-PDMS to 70% DDMPS-PDMS which can be explained due to the decrease in oxygen diffusivity in the same direction. All measurements were taken with samples initially equilibrated at 0% oxygen and exposed to air (21% oxygen) at time $t = 0$.

The percentage change in T_1 values for the liquid siloxane samples and 70% Siloxane-PDMS elastomers were plotted against the respective oxygen diffusivities in these materials (Figure 5.6). This metric, i.e., % change in T_1 can be thought of as the response sensitivity to oxygen for the different materials. The percentage change in T_1 was defined as,

$$\% \; change \; in \; T_1 = \frac{T_{1|0} - T_{1|21}}{T_{1|21}} * 100\% \tag{5.7}$$

where $T_{1|21}$ is the T_1 at 21% oxygen and $T_{1|0}$ is the T_1 at 0% oxygen. Figure 5.6 shows a clear trend of increasing % change in T_1 with oxygen diffusivities for both the liquid and solid elastomer materials. In other words, as we go from the smaller siloxane molecule HMDSO to the larger DDMPS, oxygen diffusivities decrease and are accompanied by a decrease in % change in T_1. The solid elastomer samples follow a similar trend where as we go from the sample with 70% weight fraction of the smaller siloxane HMDSO to one with the same weight fraction of DDMPS, we see a decrease in oxygen diffusivity and a decrease in % change in T_1.

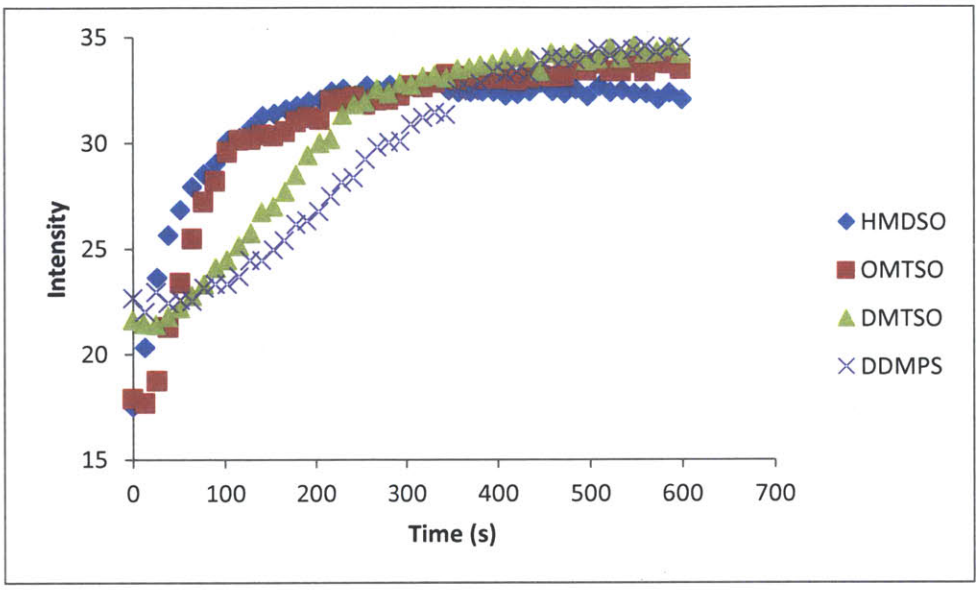

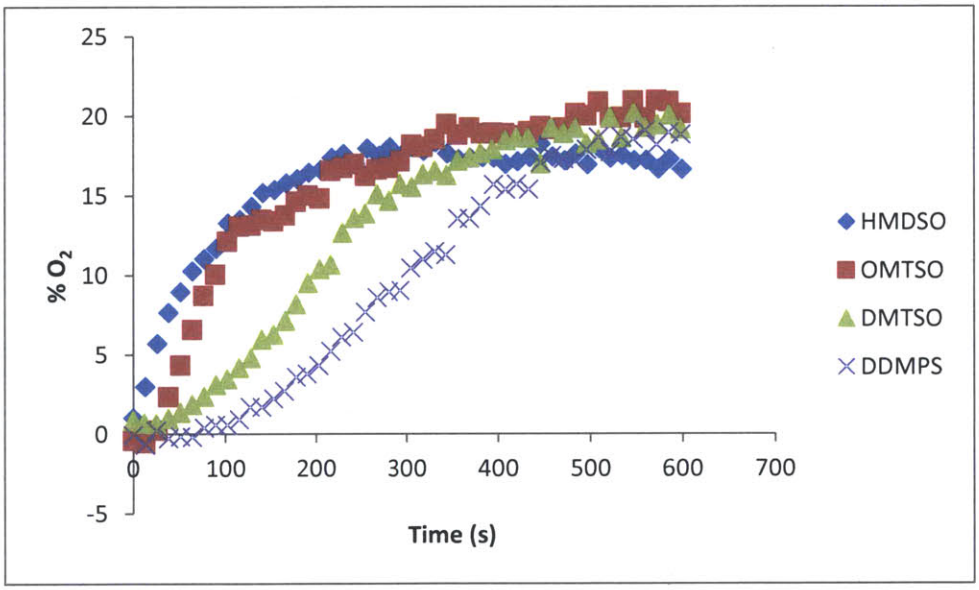

Figure 5.3 Plots showing variation in intensity (top) and percentage oxygen (bottom) for each liquid siloxane sample on the same axes.

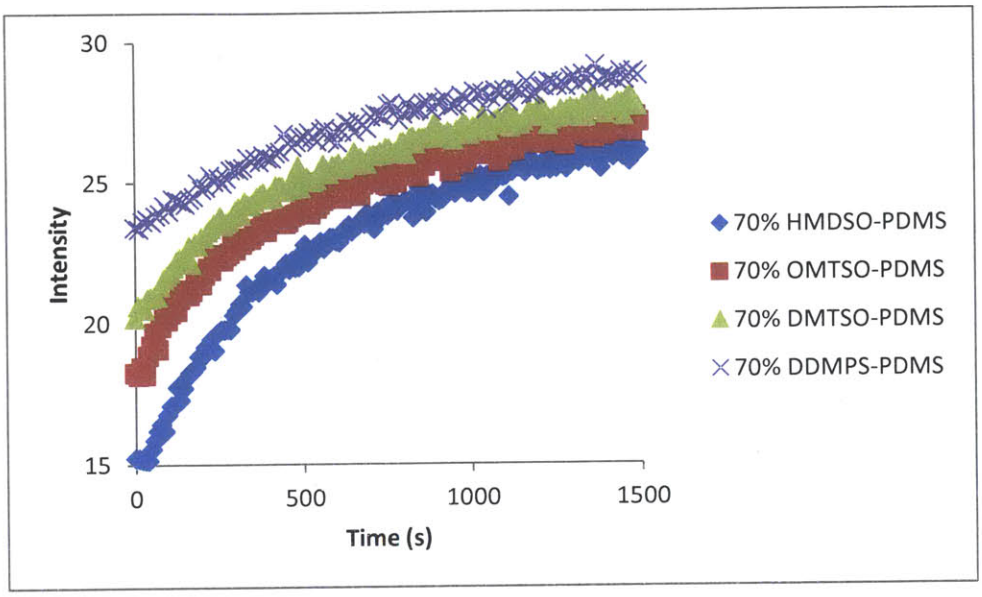

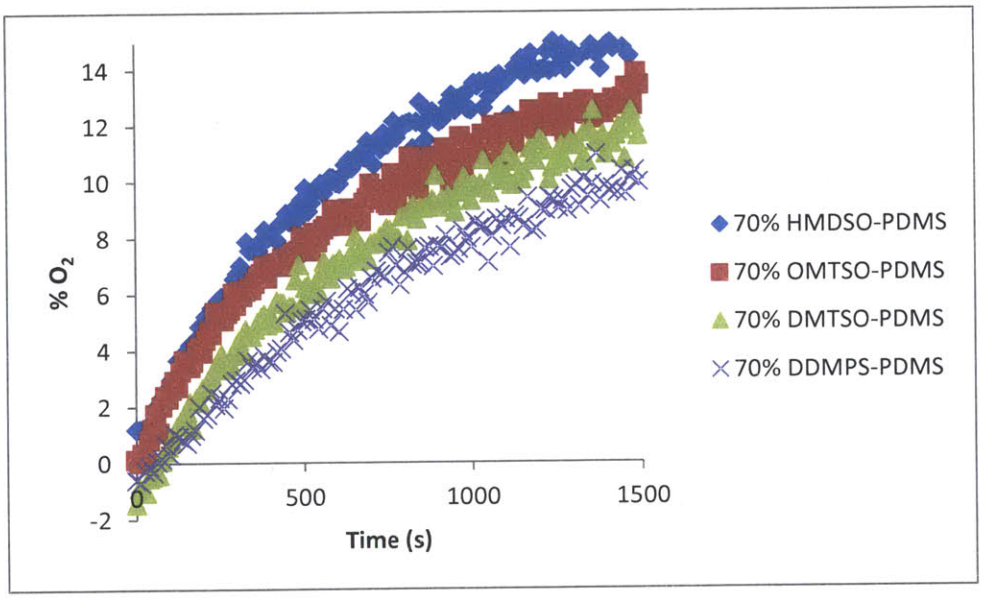

Figure 5.4 Plots showing variation in intensity (top) and percentage oxygen (bottom) for each 70% Siloxane-PDMS elastomeric solid sample on the same axes.

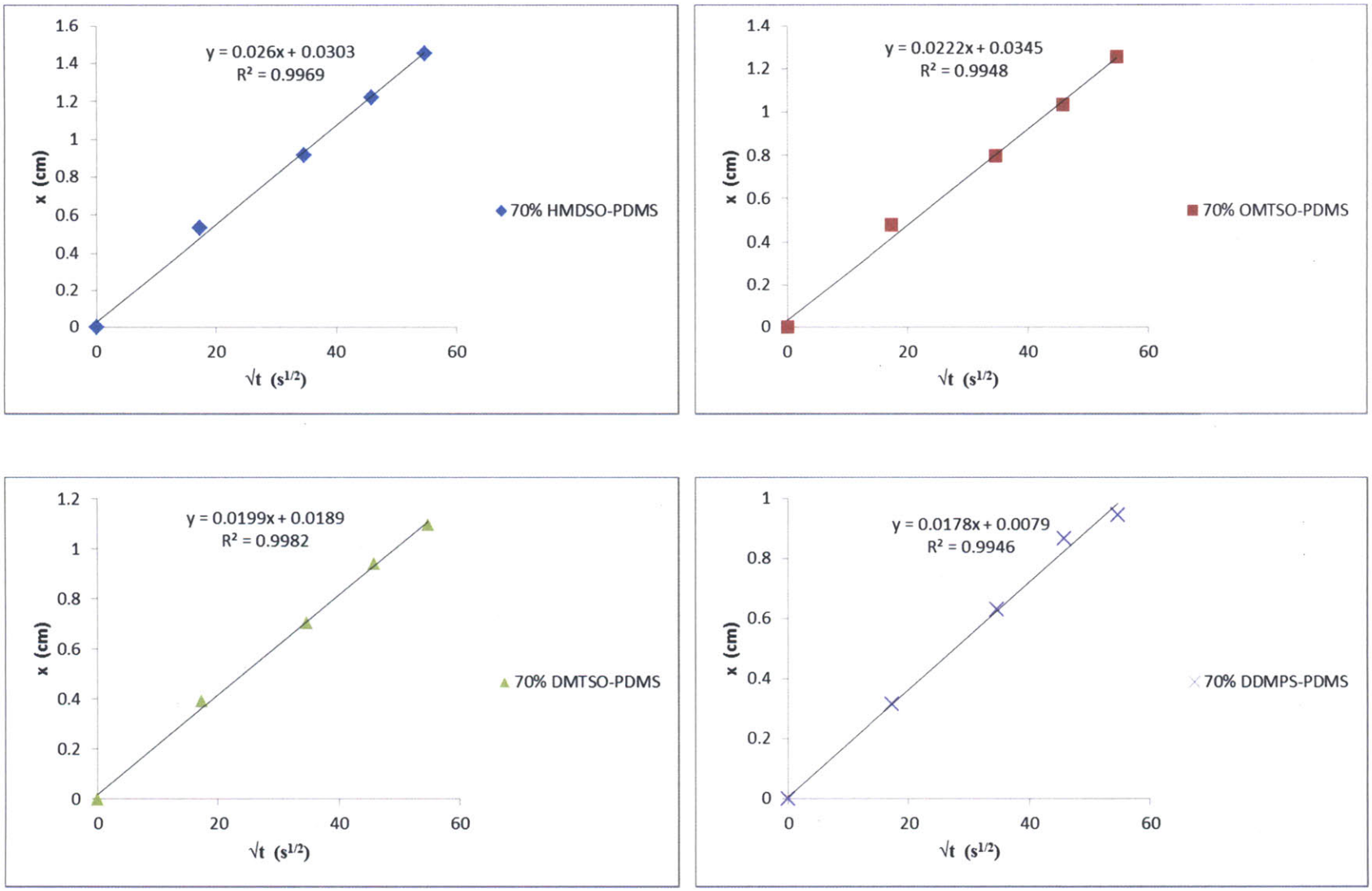

Figure 5.5 Plots of diffusion distance against the square root of time for each 70% Siloxane-PDMS sample.

Sample	Diffusivity (x 10^5 cm^2/s)
HMDSO	52.7
OMTSO	40.2
DMTSO	33.6
DDMPS	26.8
70% HMDSO-PDMS	4.22
70% OMTSO-PDMS	2.95
70% DMTSO-PDMS	2.14
70% DDMPS-PDMS	1.59
PDMS	0.316

Table 5.2 Diffusion coefficients for oxygen in each sample as obtained by fitting to the diffusion equation (Equation 5.6).

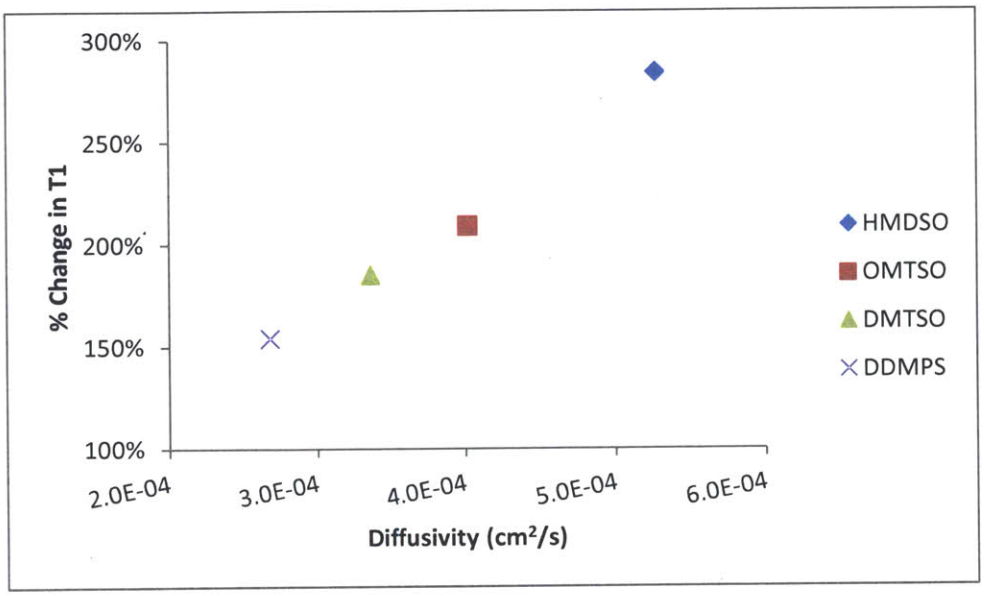

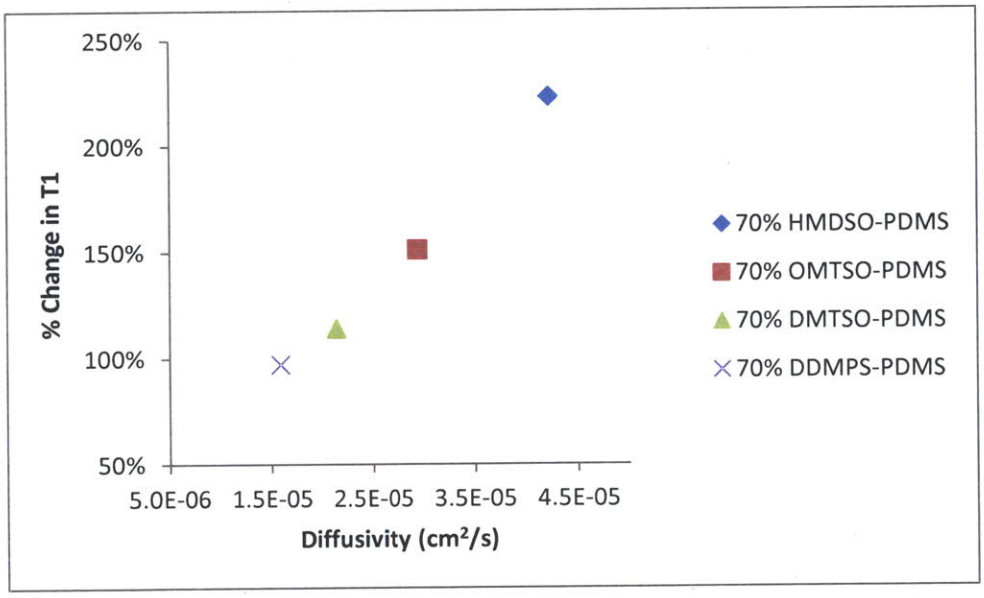

Figure 5.6 Correlation of % change in T_1 against oxygen diffusivity for liquid siloxane (top) and 70% Siloxane-PDMS (bottom) samples.

Chapter 6: *In vivo* Performance of the Injectable Polymer

A pilot animal study using an inspired gas model was conducted for the validation of *in vivo* oxygen sensing using 70% DDMPS-PDMS. The goals of this study were to determine whether 70% DDMPS-PDMS devices implanted in a live rat responded to inspired gas with varying oxygen concentrations and if the response was reversible or not.

6.1 Calibration curve for 7T MRI

Measurements and imaging were performed on a 7 T Small Animal MRI system (Varian, Inc.). Note that this field strength is much higher compared to 0.47 T, the field strength of the Bruker Minispec relaxometer at which *in vitro* measurements were made. In Chapter 3 on MR Theory, it was mentioned that the Larmor frequency of the nuclear spins is proportional to the magnetic field strength (Equations 3.1 and 3.2). This implies that at larger field strengths, the nuclear spins have a larger Larmor frequency. It will take longer for relaxation to occur at higher field strengths, i.e., a higher T_1, since T_1 involves the exchange of energy between the nuclei and surrounding lattice, and greater energy exchange is required at higher frequencies [41]. The linear calibration curve mapping the inverse of T_1 to % oxygen obtained using measurements performed on the 0.47 T Minispec is not valid for the 7 T MRI due to this increase in T_1 at higher field strengths. A separate calibration curve mapping the inverse of T_1 to the % oxygen at 7 T on the MRI was, therefore, obtained.

The MRI was first tuned to a ball containing doped water followed by frequency and power prescans using the same ball. A 70% DDMPS-PDMS disc approximately 4 mm in diameter was pushed to the base of a vial which was covered using parafilm. A thin tube connected to the output of the gas mixer system as well as a temperature probe were pushed through the parafilm and placed right over the 70% DDMPS-PDMS disc. The vial was then placed at an appropriate distance into the cradle which was then pushed into the MRI coil. This distance was chosen such that the vial was in the sensitive detection region of the coil. A fan module and heating unit were

used to heat the bore and maintain the temperature of the vial and its contents at 37°C. The VnmrJ software was used to acquire images and process data. Basic scout images were obtained to locate the vial and select an appropriate slice for imaging and T_1 mapping. The gas mixer was set to the desired oxygen concentration and the vial flushed with the particular gas mixture for 30 min before imaging. The fsems imaging protocol was then used along with inversion recovery to obtain a series of images at different TI's (inversion times) which were then processed to extract the T_1 values at the particular oxygen concentration. Figure 6.1 below shows the calibration curve and equation relating the inverse of T_1 to the oxygen concentration as measured at 7 T. This calibration curve can be used to extrapolate the oxygen concentration at a given site for a particular measured T_1 value. Note the values of the inverse of T_1 which are lower than those shown in Figure 4.8 for a 0.47 T system which is expected since the T_1 at higher field strengths is also higher.

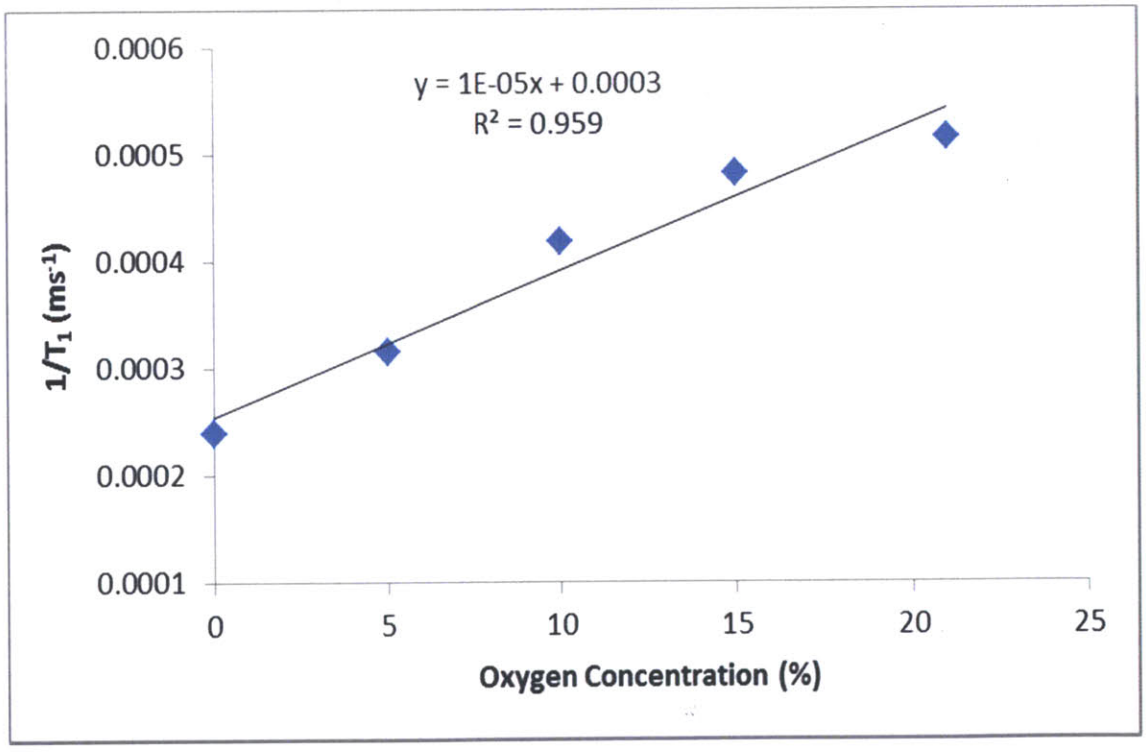

Figure 6.1 Calibration curve for 70% DDMPS-PDMS using the Varian MRI at 7 T.

6.2 *In vivo* response to changes in inspired oxygen

An inspired gas model in rodents was used to validate the response of the oxygen sensing polymer, 70% DDMPS-PDMS. The basic idea was to record changes in T_1 of a 70% DDMPS-PDMS device implanted in the hind leg muscle of a rat in response to changes in inspired oxygen. All procedures and protocols involving animals were approved by MIT's Committee on Animal Care (CAC) beforehand. The experimental protocol and the results obtained are described in detail next.

The synthesis procedure for 70% DDMPS-PDMS allows for devices of different shapes and sizes to be made as mentioned in Chapter 4. Tubular shaped devices were fabricated so that they could be easily injected using a 16.5 gauge needle. 16 gauge PTFE tubes (Small Parts Inc.) were filled with an uncured mixture of 70% DDMPS-PDMS and placed inside a petri dish. A small aluminum boat filled with pure DDMPS was also placed inside the petri dish so as to ensure that DDMPS vapors saturated the petri dish during thermal cure. The petri dish was covered and placed inside a lab oven at 80°C for 1.5 hours. Upon completion of thermal cure, the PTFE tubes were sliced open using a scalpel blade and tube-shaped 70% DDMPS-PDMS solid elastomers approximately 1 mm in diameter were extracted. A 3 mm long piece was cut out and loaded into a 16.5 gauge needle for implantation (Figure 6.2).

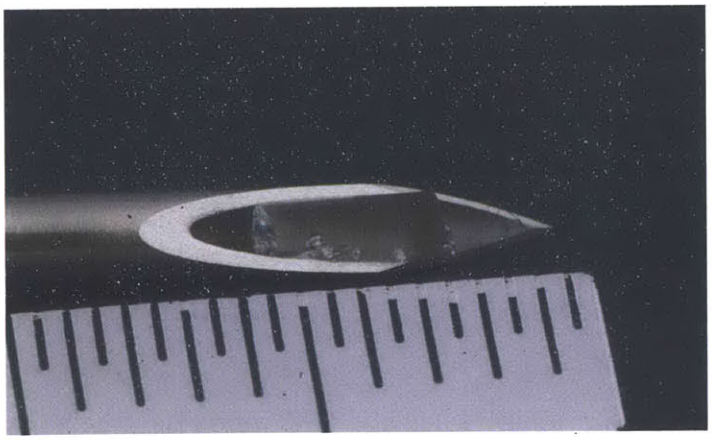

Figure 6.2 A 70% DDMPS-PDMS device (1 mm in diameter, 3 mm long) being loaded into a 16.5 gauge needle.

Each of four male, Sprague-Dawley rats weighing approximately 350 g was implanted with one 70% DDMPS-PDMS device with dimensions of 1 mm in diameter and 3 mm in length. Hair was removed from the leg in which the device was to be implanted so as to help in properly inserting the needle and injecting the device into the muscle by depressing a plunger attached to the needle. The rats were anesthetized using 1.5% isoflurane in oxygen at a flow rate of 1.5 L/min during the entire procedure. The rats were shifted to and secured in the MRI cradle once implanted with a device. Anesthesia at 1.5% isoflurane in oxygen was administered via a nose cone. Respiration rate and rectal temperature were measured using a respiration pad placed on the chest and a rectal probe respectively. Temperature was maintained at 37°C using a fan module and a heating unit.

A frequency prescan using a large ball containing doped water was performed before placing the rat inside the MRI. The rat was then placed inside the MRI and the MRI tuned to the rat followed by a power prescan routine. Basic scout images were acquired to locate the slice with the device. The T_1 value at a given inspired gas condition was evaluated by using an fsems inversion recovery sequence with images acquired at multiple *TI*'s. The high T_2 value for the 70% DDMPS-PDMS material allowed acquisition of images at higher TE's (echo times).This enabled suppression of the water signal from adjacent tissue as can be seen in Figure 6.3. A baseline measurement with oxygen as the inspired gas was taken initially following which the anesthesia carrier gas, and hence the inspired gas, was switched to medical air (21% oxygen). 20 minutes after switching the inspired gas, multiple measurements for T_1 were taken so as to ensure that the value had stabilized. The anesthesia carrier gas was then switched back to oxygen and once again multiple T_1 measurements were taken 20 minutes after the switch. Isoflurane was dialed down to 0% upon completion of measurements and the rats were allowed to breathe oxygen with warm air blowing over them until they recovered from anesthesia. Figure 6.3 shows the results from this pilot study. The *in vivo* response of the devices was as expected. Higher oxygen content led to a lower T_1 value and higher image intensity whereas lower oxygen content (air) resulted in a lower T_1 and therefore lower image intensity. The response was found to be completely reversible as well.

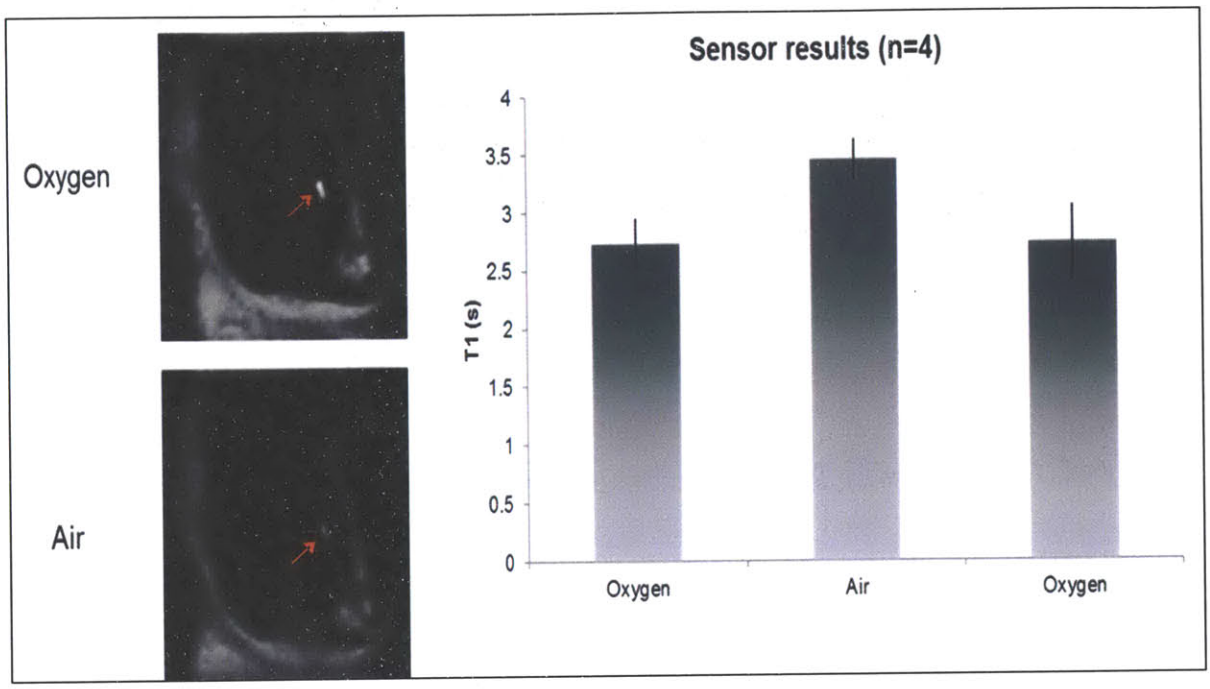

Figure 6.3 MRI images of the 70% DDMPS-PDMS device implanted in the hind leg muscle of a rat and the T_1 response to inspired gas with different oxygen concentration.

Chapter 7: Conclusion and Future Work

7.1 Conclusion

The work presented in this thesis has detailed the synthesis and characterization of a polymer, 70% DDMPS-PDMS, which responds to oxygen by altering its longitudinal relaxation time constant T_1 (an MR property). This solid elastomeric material is comprised of a blend of two siloxanes, DDMPS and PDMS, in a specific weight ratio. DDMPS is the component that confers oxygen sensitivity whereas PDMS provides structural integrity to the polymer. The synthesis procedure allows for easy molding of the polymer into various shapes and sizes. *In vitro* measurements showed that the material had a large dynamic range especially in the physiologically relevant oxygen concentration ranges. T_1 response to oxygen was found to be completely reversible. The specificity of response to oxygen was tested by measuring the T_1 response to carbon dioxide, the other major gas found in blood and hence the body. The measurements obtained showed no difference in T_1 between 0% and 100% carbon dioxide thus establishing that 70% DDMPS-PDMS does not respond to carbon dioxide.

DDMPS belongs to the family of linear siloxanes also including HMDSO, OMTSO and DMTSO. All of these siloxanes show large T_1 changes in response to changes in oxygen levels. Oxygen diffusivities of these four liquid siloxanes as well as their solid elastomer 70% Siloxane-PDMS counterparts were measured in order to better understand the underlying mechanisms behind the different T_1 responses to oxygen for each of these materials. Intensity based MR measurements at a specific depth of sample were taken upon exposing samples initially equilibrated at 0% oxygen to air. Intensity time-course measurements were converted to percentage oxygen time-course using the saturation recovery and $1/T_1$ vs. % oxygen calibration equations. The oxygen diffusivities for the liquid siloxanes and their 70% Siloxane-PDMS solid counterparts were correlated against the oxygen response sensitivities as represented by percentage change in T_1 to oxygen. It was found that larger oxygen diffusivities corresponded to larger percentage changes in T_1 response for both the liquid and solid siloxane materials.

The 70% DDMPS-PDMS material was tested *in vivo* by recording the changes in T_1 of a device implanted in the hind leg of a rat in response to inspired gas of varying oxygen concentrations. A tubular shaped device, 1 mm in diameter and 3 mm long, was obtained using a 16 gauge PTFE tube as a mold. In each of four rats, a single device was injected in the hind leg using a 16.5 gauge needle. Inspired gas was varied by cycling the anesthesia carrier gas from oxygen to air and back to oxygen. T_1 measurements taken using a 7 T MRI system were as expected with a higher oxygen content resulting in a lower T_1 and a higher image intensity, and vice versa. The response was found to be completely reversible as well.

7.2 Recommendation for future studies

Alternative formulations of the 70% DDMPS-PDMS material may be considered so as to further ease sensor implantation *in vivo* without comprising the T_1 response to oxygen. One such formulation could be a suspension of 70% DDMPS-PDMS microparticles in water. Although mechanisms of microparticle agglomeration into a solid depot *in vivo* will need to be investigated, this could be a particularly attractive proposition given that a much finer gauge needle could be used. Siloxane based chemistries may further be explored to achieve covalent cross-linking of oxygen sensitive siloxanes to a PDMS or PDMS-like backbone. Such a covalently bound, cross-linked polymer would have the advantage of being thermally stable and without the potential issue of losing the volatile oxygen sensitive components over longer periods of time.

A pilot study of the *in vivo* T_1 response to inspired gas with varying oxygen concentrations directly after implantation was presented in this thesis. A longer study is underway which would enable us to track the changes in T_1 response to inspired oxygen over time. Such a study would be helpful in assessing the stability of the device (response) for longer implantation times. The effect of the device on surrounding tissue due to a long-term implant will also be studied via histology upon completion of the study. Animal models for compartment syndrome and tumor hypoxia will need to be developed in the future so as to test the performance of the material for oxygen sensing in these clinically important conditions as well.

References

[1] R.M. Leach and D.F. Treacher. "Tissue Hypoxia." *British Medical Journal*, vol. 317, pp. 1370-1373, 1998.

[2] H.K. Said, N.K. Roy, A.N. Gurjala, and T.A. Mustoe. "Quantifying tissue level ischemia: hypoxia response element-luciferase transfection in a rabbit ear model." *Wound Repair and Regeneration*, vol. 17, pp. 473-439, 2009.

[3] "Compartment syndrome (CS) and the role of fasciotomy in extremity war wounds," in the Joint Theater Trauma System Clinical Practice Guideline. [Online]. Available: www.usaisr.amedd.army.mil/assets/cpgs/Compartment_Syndrome_and Fasciotomy_9_Mar_12.pdf . March, 2012.

[4] M. T. Jobe. "Compartment syndromes and Volkmann contracture," in *Campbell's Operative Orthopaedics*, 11th ed., vol. 4. S.T. Canale and J.H. Beaty, Ed. Philadelphia: Mosby, 2008, pp. 4259-4273.

[5] C. Middleton. "Compartment syndrome: the importance of early diagnosis." *Nursing Times*, vol. 99, pp. 30-32, 2003.

[6] K.G.B. Elliott and A.J. Johnstone. "Diagnosing acute compartment syndrome." *Journal of Bone & Joint Surgery*, vol. 85, pp. 625-632, 2003.

[7] A. Seekamp, M. Van Griensven, H. Blankenburg and G. Regel. "Intramuscular partial oxygen tension monitoring in compartment syndrome—an experimental study." *European Journal of Emergency Medicine*, vol. 4, pp. 185-192, 1997.

[8] P. Vaupel and L. Harrison. "Tumor hypoxia: causative factors, compensatory mechanisms, and cellular response." *The Oncologist*, vol. 9, pp. 4-9, 2004.

[9] L.B. Harrison, M. Chadha, R.J. Hill, K. Hu and D. Shasha. "Impact of tumor hypoxia and anemia on radiation therapy outcomes." *The Oncologist*, vol. 7, pp. 492-508, 2002.

[10] J.Z. Wang, X.A. Li and N.A. Mayr. "Dose escalation to combat hypoxia in prostate cancer: a radiobiological study on clinical data." *British Journal of Radiology*, vol. 79, pp. 905-911, 2006.

[11] P.W. Vaupel, D.K. Kelleher and M. Gunderoth, Ed. *Tumor Oxygenation*. New York: Fischer, 1995.

[12] H.B. Stone, J.M. Brown, T.L. Phillips and R.M. Sutherland. "Oxygen in human tumors: correlations between methods of measurement and response to therapy." *Radiation Research*, vol. 136, pp. 422-434, 1993.

[13] E.F. Di Martino, B. Gagel, O Schramm, P. Maneschi and M. Westhofen. "Evaluation of tumor oxygenation by color duplex sonography: a new approach." *Otolaryngology Head & Neck Surgery*, vol. 132, pp. 765-769, 2005.

[14] P. Vaupel, K. Schlenger, C. Knoop and M. Hockel. "Oxygenation of human tumors: evaluation of tissue oxygen distribution in breast cancers by computerized O_2 tension measurements." *Cancer Research*, vol. 51, pp. 3316-3322, 1991.

[15] B. Movsas, J.D. Chapman, A.L. Hanlon, E.M. Horwitz, W.H. Pinover, R.E. Greenberg, C. Stobbe and G.E. Hanks. "Hypoxia in human prostate carcinoma: an Eppendorf pO_2 study." *American Journal of Clinical Oncology*, vol. 24, pp. 458-461, 2001.

[16] R.A. Gatenby, H.B. Kessler, J.S. Rosenblum, L.R. Coia, P.J. Moldofsky, W.H. Hartz and G.J. Broder. "Oxygen distribution in squamous cell carcinoma metastases and its relationship to outcome of radiation therapy." *International Journal of Radiation Oncology Biology Physics*, vol. 14, pp. 831-838, 1988.

[17] C. Bittenbender. "Compartment syndrome vs. crush syndrome," presented at the 10th Int. Conf. NCEMSF, Washington D.C., USA, 2003.

[18] D.E. Detmer, K. Sharpe, R.L. Sufit and F.M. Girdley. "Chronic compartment syndrome: diagnosis, management, and outcomes." *American Journal of Sports Medicine*, vol. 13, pp. 162-170, 1985.

[19] R.B. Heppenstall. "An update in compartment syndrome investigation and treatment." *University of Pennsylvania Orthopedic Journal*, vol. 10, pp. 49-57, 1997.

[20] L.R. Mohler, J.R. Styf, R.A. Pedowitz, A.R. Hargens and D.H. Gershuni. "Intramuscular deoxygenation during exercise in patients who have chronic anterior compartment syndrome." *Journal of Bone & Joint Surgery*, vol. 79, pp. 844-849, 1997.

[21] A. Uliasz, J.T. Ishida, J.K. Fleming and L.G. Yamamoto. "Comparing the methods of measuring compartment pressured in acute compartment syndrome." *American Journal of Emergency Medicine*, vol. 21, pp. 143-145, 2003.

[22] J.D. Chapman, L.R. Coia, C.C. Stobbe, E.L. Engelhardt, M.C. Fenning and R.F. Schneider. "Prediction of tumor hypoxia and radioresistance with nuclear medicine markers." *British Journal of Cancer*, vol. 74, pp. S204-S208.

[23] J. Jiang, L. Gao, W. Zhong, S. Meng, B. Yong, Y. Song, X. Wang and C. Bai. "Development of fiber optic fluorescence oxygen sensor in both *in vitro* and *in vivo* systems." *Respiratory Physiology & Neurobiology*, vol. 161, pp. 160-166, 2008.

[24] X. Xiong, D. Xiao and M.M. Choi. "Dissolved oxygen sensor based on fluorescence quenching of oxygen-sensitive ruthenium complex immobilized on silica-Ni-P composite coating." *Sensors and Actuators B*, vol. 117, pp. 172-176, 2006.

[25] D.F. Wilson, S. Gomi, A. Pastuszko and J.H. Greenberg. "Microvascular damage in the cortex of cat brain from middle cerebral artery occlusion and reperfusion." *Journal of Applied Physiology*, vol. 74, pp. 580-589, 1993.

[26] P. Babilas, P. Lamby, L. Prantl, S. Schreml, E.M. Jung, G. Liebsch, O.S. Wolfbeis, M. Landthaler, R.M. Szeimies and C. Abels. "Transcutaneous pO2 imaging during tourniquet-induced forearm ischemia using planar optical oxygen sensors." *Skin Research and Technology*, vol. 14, pp. 304-311, 2008.

[27] B.B. Williams, N. Khan, B. Zaki, A. Hartford, M.S. Ernstoff and H.M. Swartz. "Clinical electron paramagnetic resonance (EPR) oximetry using India ink." *Advanced Experimental Medical Biology*, vol. 662, pp. 149-156, 2010.

[28] S. Hunjan, R.P. Mason, A. Constantinescu, P. Peschke, E.W. Hahn and P.P. Antich. "Regional tumor oximetry" ^{19}F NMR spectroscopy of hexafluorobenzene." *International Journal of Radiation Oncology Biology Physics*, vol. 41, pp. 161-171, 1998.

[29] K. Golman, L.E. Olsson, O. Axelsson, S. Mansson, M. Karlsson and J.S. Petersson. "Molecular imaging using hyperpolarized ^{13}C." *British Journal of Radiology*, vol. 76, pp. S118-S127, 2003.

[30] Y. Wu, T.G. Reese, H. Cao, M.I. Hrovat, S.P. Toddes, R.A. Lemdiasov and J.L. Ackerman. "Bone mineral imaged in vivo by ^{31}P solid state MRI of human wrists." *Journal of Magnetic Resonance Imaging*, vol. 34, pp. 623-633, 2011.

[31] "Pure silicone fluid 2cSt dodecamethylpentasiloxane," in CLEARCO Product Information Catalogue. [Online]. Available: www.clearcoproducts.com/pdf/volatile/NP-PSF-2cSt.pdf . (Accessed Dec. 2012).

[32] Y. Ling, T. Pong, C. Vassiliou, P.L. Huang and M.J. Cima. "Implantable magnetic relaxation sensors measure cumulative exposure to cardiac biomarkers." *Nature Biotechnology*, vol. 29, pp. 273-277, 2011.

[33] J. Curtis and A. Colas. "Medical applications of silicones," in Biomaterials Science, 2nd ed. B.D. Ratner, A.S. Hoffman, F.J. Schoen and J.E. Lemons, Ed. Philadelphia: Elsevier, 2004, pp. 697-707.

[34] "Blood gases," on MedLine Plus, U.S. National Library of Medicine, National Institutes of Health. [Online]. Available: www.nlm.nih.gov/medlineplus/ency/article/003855.htm . (Accessed Dec. 2012).

[35] H. Zhang and A. Cloud. "The permeability characteristics of silicone rubber," presented at SAMPE Fall Technical Conf., Dallas, TX, 2006.

[36] S. Chowdhury, V.R. Bhethanabotla and R. Sen. "Measurement of diffusion coefficient of oxygen in FRP using luminescence quenching," presented at ACMA Composites & Polycon, Tampa, FL, 2007.

[37] T.Y. Katircioglu, H.Y. Kaptan and O. Guven. "Determination of oxygen diffusion coefficient of poly(methacrylonitrile) II and the calculation of diffusion activation energy." *Journal of Applied Polymer Science*, vol. 74, pp. 1108-1118, 1999.

[38] K.F. Webb and A.S. Teja. "Solubility and diffusion of carbon dioxide in polymers." *Fluid Phase Equilibria*, vol. 158, pp. 1029-1034, 1999.

[39] J. Crank. *The Mathematics of Diffusion*. Oxford, UK: Oxford, 1956.

[40] J. Crank. *The Mathematics of Diffusion*. Oxford, UK: Oxford, 1975.

[41] D.G. Nishimura. *Principles of Magnetic Resonance Imaging*. CA, USA: Lulu, 2010.